UNIVERSITAT POLITÈCNICA
DE CATALUNYA
BARCELONATECH

Cylindrical microplane model for fiber reinforced polymer composites

Saeed Sabounchi

ADVERTIMENT La consulta d'aquesta tesi queda condicionada a l'acceptació de les següents condicions d'ús: La difusió d'aquesta tesi per mitjà del repositori institucional UPCommons (http://upcommons.upc.edu/tesis) i el repositori cooperatiu TDX (http://www.tdx.cat/) ha estat autoritzada pels titulars dels drets de propietat intel·lectual **únicament per a usos privats** emmarcats en activitats d'investigació i docència. No s'autoritza la seva reproducció amb finalitats de lucre ni la seva difusió i posada a disposició des d'un lloc aliè al servei UPCommons o TDX. No s'autoritza la presentació del seu contingut en una finestra o marc aliè a UPCommons (*framing*). Aquesta reserva de drets afecta tant al resum de presentació de la tesi com als seus continguts. En la utilització o cita de parts de la tesi és obligat indicar el nom de la persona autora.

ADVERTENCIA La consulta de esta tesis queda condicionada a la aceptación de las siguientes condiciones de uso: La difusión de esta tesis por medio del repositorio institucional UPCommons (http://upcommons.upc.edu/tesis) y el repositorio cooperativo TDR (http://www.tdx.cat/?locale-attribute=es) ha sido autorizada por los titulares de los derechos de propiedad intelectual **únicamente para usos privados enmarcados** en actividades de investigación y docencia. No se autoriza su reproducción con finalidades de lucro ni su difusión y puesta a disposición desde un sitio ajeno al servicio UPCommons No se autoriza la presentación de su contenido en una ventana o marco ajeno a UPCommons (*framing)*. Esta reserva de derechos afecta tanto al resumen de presentación de la tesis como a sus contenidos. En la utilización o cita de partes de la tesis es obligado indicar el nombre de la persona autora.

WARNING On having consulted this thesis you're accepting the following use conditions: Spreading this thesis by the institutional repository UPCommons (http://upcommons.upc.edu/tesis) and the cooperative repository TDX (http://www.tdx.cat/?locale- attribute=en) has been authorized by the titular of the intellectual property rights **only for private uses** placed in investigation and teaching activities. Reproduction with lucrative aims is not authorized neither its spreading nor availability from a site foreign to the UPCommons service. Introducing its content in a window or frame foreign to the UPCommons service is not authorized (framing). These rights affect to the presentation summary of the thesis as well as to its contents. In the using or citation of parts of the thesis it's obliged to indicate the name of the author.

UNIVERSITAT POLITÈCNICA DE CATALUNYA

Doctoral dissertation

Nuclear and ionizing radiation engineering program

Cylindrical Microplane Model for Fiber Reinforced Polymer Composites

Author:	*Supervisor:*
Saeed Sabounchi	Prof. Ferhun Cem Caner Baskurt

July 2022

Abstract

Fiber-reinforced polymers (FRPs) are the most used composite materials in many applications, from broom handle to the main structure of advanced aircraft. Despite the enormous research done on these materials, many aspects of their behavior need more study. The progress of computers and their calculation power provides opportunities for developing new constitutive models with more capability in terms of accuracy and applicability. On the one hand, most of the existing models are limited to the specific loading situations and cannot perform beyond the limitations in the loading path. Furthermore, these models have not been sufficiently verified in general three-dimensional loading condition. This study presents a constitutive model based on microplane approach in which a cylindrical geometry is adopted for general three-dimensional stress analysis of transversely isotropic fiber-reinforced polymers. The axis of the cylinder coincides with the fibers direction in the lamina, which allows decoupling of fiber and matrix behaviors. The model has been easily implemented in finite element software called Abaqus/Explicit using the VUMAT interface. Unlike the other microplane models for predicting fracture and behavior of fiber-reinforced polymers, this model is more intuitive and easier to calibrate. The microplane constitutive laws between microplane stress and strain components are developed for inelastic and fracturing behavior of such materials in tension, compression, and shear. The micro-macro stress equilibrium equation for the cylindrical geometry is employed to calculate the macroscopic stress tensor using the microplane stress components. An explicit computational algorithm for the cylindrical microplane model is developed. A user-friendly calibration procedure is presented for adjustable parameters in the microplane constitutive laws. The full calibration of the model needs simple uniaxial test data in tension and compression in the isotropy plane and in the fiber direction for any given fiber-reinforced polymer. The model is calibrated using experimental data obtained from literature for four different types of fiber reinforced polymer composites. The model is verified using biaxial failure envelopes and 3 point bending size effect tests obtained from literature.

Keywords:

Fiber reinforced polymer, microplane model, constitutive behavior, fracture, strain-softening, finite element analysis, VUMAT

Dedication

This thesis is dedicated to my lovely wife. She has supported and encouraged me during the challenges and hardships of this work. I am truly thankful for having her in my life. This work is also dedicated to my parents, who have always loved and supported me unconditionally. As honorable, kind, and honest persons, they are my role models in life.

Acknowledgement

Above all, I would like to express my sincere appreciation to my research supervisor, Professor Ferhun Cem Caner Baskurt for the main idea of this research, his excellent guidance, decisive role in writing and publishing the paper and thesis, and support during my PhD study.

Funding:

This research did not receive any specific grant from funding agencies in the public, commercial, or not-for-profit sectors.

Contents

Chapter 1

Introduction

The fiber-reinforced polymer composite materials (FRPs), known also as advanced composites, have progressed from an engineering curiosity to a widely used material in today's applications. The composite material signifies that two or more materials are combined at a macroscopic scale to form a useful third material. The main point is that the components can be identified separately at the macroscopic scale in the structure of composite material. The main advantage of the composites is well-designed and fabricated composites can exhibit at least the strength of their components and some additional advantages in properties that none of the ingredients possess. The properties that composite materials can improve are: (1) Density, (2) electrical properties, (3) mechanical properties, and (4) heat conduction properties. Undoubtedly, some of the properties are mutually exclusive [1]. The beginning of the composite history is not known precisely, but judging from the use of straws to strengthen mud bricks and the use of plywood by ancient Egyptians, the history of composite materials is rather long [2]. There are different classifications for composites in many sources but the most commonly accepted one divides composites into four groups: (1) Fibrous composites, (2) laminated composites, (3) particulate composites, and (4) combination of these three types. Composite materials have mechanical behavior significantly different from conventional materials. Efficient engineering design requires a stiff, strong, and ductile material as the conventional steel but much lighter in weight. An accurate mechanical model for the behavior of these composites that considers the material behavior in all regimes, such as elastic, plastic, and fracturing, including the localization of fracture into a band of finite width, is needed in engineering design for use in the calculations by the finite element method. Although several tensorial models have been developed to model such behavior, the success of these models and their versatility has been lacking. By contrast, the microplane models have been developed for many different materials with great versatility and data fitting capabilities due to the reduction of strict second-order tensorial relations to more flexible first-order tensorial relations.

For example, several versions of the microplane models for concrete have been used in the commercial software package Atena [3]. In this study, a new, more intuitive microplane model, called the Cylindrical Microplane Model for Transversely Isotropic Fiber-reinforced Polymer Composites, is presented as a capable mechanical model for modeling the mechanical behavior of such materials under general 3D states of stress. Initially, the model is developed for a cylindrical geometry to capture the anisotropy of unidirectional fiber-reinforced polymers but it can be extended to the multidirectional laminated and braided fiber-reinforced composites. Chapter 1 presents the concepts of the model along with a literature survey. It has three parts. The first part covers the fundamental mechanical behavior of fiber-reinforced composites. The second part reviews fracture of fiber-reinforced polymers, and finally, the last part is a literature survey of the microplane models. Chapter 2 describes the cylindrical microplane model for transversely isotropic fiber-reinforced polymers. In this chapter, first, the basic concept of the model and subsequently the formulation of the model are illustrated. In Chapter 3, the constitutive model driver for one Gauss point and the development of microplane stress-strain boundaries are presented. Finally, the VUMAT Abaqus user material subroutine for the model is presented. In Chapter 4, the finite element simulations using the VUMAT user subroutine are compared to experimental data for both calibration and verification purposes. Furthermore, a detailed procedure for the calibration of the model parameters is presented.

Chapter 2

Basic Concepts and Literature Survey

2.1 Composite Material

A composite material is made up of two or more macroscopic level materials as its constituents that are visually distinguishable unlike in alloys in which one or more constituent materials are found in the form of a solid solution. In composites, there are reinforcing materials which are embedded in the material called the matrix. Steel reinforced concrete and graphite fiber reinforced polymers are examples of two composites materials. The basic concept of the mechanics of composite materials is divided into two points of view: (1) Micromechanics, (2) Macromechanics. These points of view allow tailoring and fitting a composite material to the engineering requirements. The Micromechanics view advocates that the lamina properties can be experimentally determined or mathematically estimated on the basis of the basic properties of the combined materials. In this view properties and behavior of the lamina can be predicted by the properties and interaction of constituent materials which is essential in making and designing composites. Thus micromechanics becomes more important when the material design is prioritized rather than structural analysis. The Micromachanics approach helps enhance the fatigue behavior of FRPs [4]. In composite materials, the high stiffness and strength required may be achieved in all directions as in isotropic composites, e.g. fiber reinforced concrete, or they may be achieved in some specific directions as in orthotropic composites, e.g. FRP composite laminates. In Macromechanics approach [5] the anisotropic laminas are stacked in several directions so as to satisfy the need for high stiffness and strength requirements in several directions resulting in thick laminates. The laminate becomes approximately isotropic in the plane of the lamina when many lamina in almost all directions are stacked together. The laminate, therefore, is the result of manufacturing two or more layers from the same composite in different directions bonded together typically by the matrix but in some cases by stitching also. Figure 2.1 shows the concept of laminate [6].

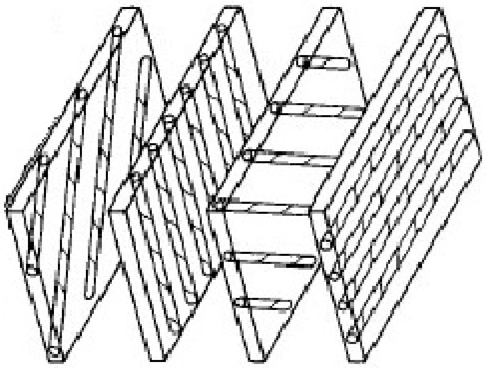

Figure 2.1: Laminate obtained from stacking 5 laminas in different directions, taken from [7]

The stacking of laminas can also be achieved by weaving as shown in Figure 2.2

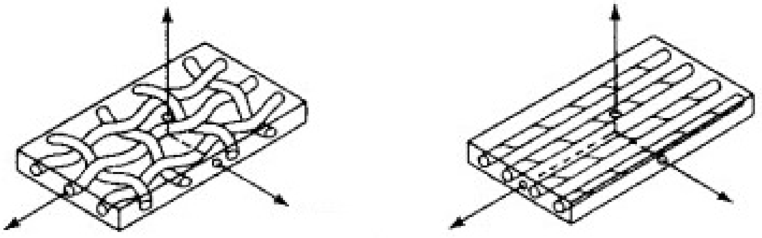

Figure 2.2: Woven Fibers (Left) and Unidirectional Fibers (Right) , taken from [7]

The main aim of lamination is to reduce the directional dependence of strength and stiffness in the composite. Laminates are uniquely suitable for the directional loading environments because the direction of each layer can be matched according to necessity. For example, six layers of a ten-layer laminate in one direction and the other four at 90° to that direction; can present a laminate with strength and extensional stiffness roughly 50 % higher in one direction than the other [8]. The ratio of the tensile stiffnesses in the two directions can reach 4 to 6 [6]. As it was mentioned, fibers have the role of reinforcing material in the mechanical performance of composites. The fibers affect the mechanical properties of the composites in the following ways:

1. The first obvious factor is the mechanical properties of the fiber material itself. The strength and stiffness of the fibers are expected to be high so as to increase the strength and stiffness of the composite. Furthermore, the cost of the fibers is an essential point that makes graphite, glass, and aramids dominate the fiber market.

2. The shape of the fibers is another factor that can affect the mechanical performance of composites. The fibers' shape can be circular, hexagonal, and square, but the most common shape is circular. Higher strength and stiffness are achieved through better packing in the case of hexagonal and square fibers. However, cir-

cular fibers are still preferred because of their ease of handling and manufacturing.

3. Length of fiber affects composite mechanics. The fibers can be short or long. Long fibers can easily be oriented properly but short fibers are harder to orient correctly. Furthermore, high impact resistance, low shrinkage, improved surface finish, and better dimensional stability are advantages of long fibers over the short ones. On the other hand, the short fibers cost less and they are easier to work with. Also, due to the fewer flaws in short fibers, they have higher strength.
4. Fiber orientation is another important factor that affects the stiffness and strength of composites. Fibers in composites can be unidirectional or multidirectional. Unidirectional fiber composites have very high stiffness and strength in the longitudinal (fiber) direction. If fiber directions are more than one, the composite has higher overall stiffness and strength. However, unidirectional fiber composites have higher stiffness and strength than multidirectional fiber composites for the same volume of fibers.

The matrix is the constituent in composite materials that binds fibers together and distributes the load to fibers. It also has the role of a protective shield for the fibers. Matrix materials have much lower mechanical performance than fiber, but the mechanical properties of composites are highly dependent on those of the matrix. Transverse and shear moduli, interlaminar shear strength, transverse strength, fatigue strength, and compressive strength directly influenced by the stiffness and the strength of the matrix. In addition, the mechanical properties of the fiber-matrix interface influence critically the mechanical performance of composites because those properties dictate how well the load is distributed across the fibers by the matrix. There are three types of bonding in fiber-matrix interfaces, and mostly more than one bonding type occurs simultaneously: Chemical bonding, mechanical bonding and reaction bonding. Chemical bonding occurs between the surface of fibers and the matrix. Some fibers can bond to the matrix by themselves or specific compounds called coupling agents applied to the surface of fibers can be employed to create better chemical bonding. The roughness of the fiber surface gives rise to mechanical bonding between the fiber surface and matrix. The fiber surface mechanically locks into the matrix, and a mechanical bond is formed. Reaction bonding occurs due to matrix thermal expansion coefficient being higher than fiber thermal expansion coefficient and the manufacturing temperature being higher than the operating temperature. Upon cooling, the matrix shrinks more than fibers and compresses them together. The disadvantage of this bonding is that microcracks can be formed in both the fiber and the matrix which in turn can lead to diminished composite strength [9]. The stress-strain behavior of the composite constituents may be divided into four classes as depicted in Figure 2.3 . Fibers generally exhibit brittle linear elastic behavior. Some composite materials with polymers and aluminum have a nonlinear stress-strain curve. Generally, resinous matrix materials behave in visco-elasto-plastic range. Thus, the nonlinear stress response of these composites also depends on strain rate.

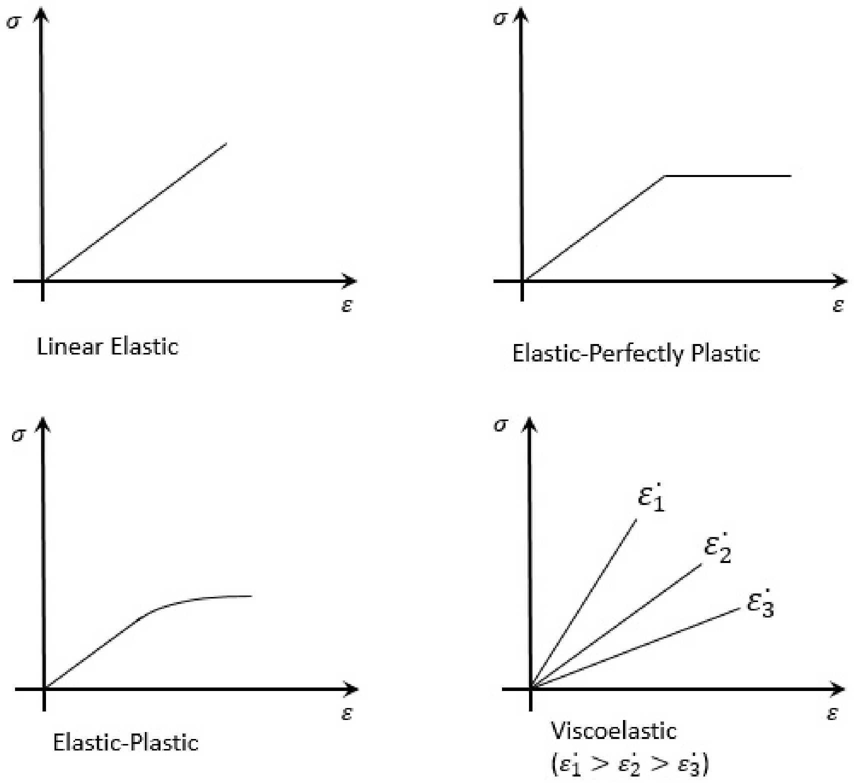

Figure 2.3: Various Stress-Strain Behaviors , taken from [7].

2.2 Fiber Reinforced Polymers

The FRPs are the most used among the advanced composites. In such composites polymer matrix such as epoxy or urethane is reinforced by long fibers made of graphite, aramid, boron, carbon or glass. FRPs have notably high strength to weight ratio and lower cost than most comparable alloys. Carbon fiber/epoxy composites have approximately five times higher strength to weight ratio than ordinary steels. Furthermore, simpler manufacturing and lower cost than other composites makes them the most common composites. However, low operating temperatures and high thermal expansion coefficient are the main weak points of FRPs. FRPs are widely used in different applications from simple sports tools to advanced spacecraft. From the fracture mechanics point of view, FRPs are quasi-brittle materials. In these materials, fracture is the main cause of the failure (rather than plastic slip which is often the case in polymers and metals). A significantly large fracture-process zone surrounds the fracture tip. In this zone micro-cracking and damage occurs. The brittle material is a special case of the quasi-brittle materials, for which the fracture-process zone (FPZ) become negligibly small compared to the size of the structure. Linear elastic fracture mechanics can be used to analyze the brittle elastic materials but for a general quasi-brittle structure, nonlinear fracture mechanic is required due to non-negligible size of the FPZ [10]. Most of the existing models for the fracture of the quasi-brittle materials [11, 12, 13] include neither the predictive capabilities in general multiaxial loading in 3D nor the capability to predict post-peak fracturing behavior [14].

2.3 Macromechanical Behavior of Lamina

In Cartesian coordinates, the elastic stress-strain relation in tensor form for general anisotropic material is given by:

$$\sigma_{ij}= s_{ijkl}\,\epsilon_{kl} \tag{2.1}$$

where σ_{ij} are the components of the 2nd order stress tensor, ϵ_{kl} are the components of the 2nd order strain tensor and s_{ijkl} are the components of the 4th order stiffness tensor (indices i, j, k and l vary from 1 to 3). The tensor components σ_{ij} and ϵ_{kl} form symmetric tensors and thus they can be expressed in Voigt notation in the form of vectors to yield the matrix equations

$$\begin{bmatrix}\sigma_{11}\\\sigma_{22}\\\sigma_{33}\\\sigma_{12}\\\sigma_{23}\\\sigma_{13}\end{bmatrix}=\begin{bmatrix}S_{11} & S_{12} & S_{13} & S_{14} & S_{15} & S_{16}\\S_{12} & S_{22} & S_{23} & S_{24} & S_{25} & S_{26}\\S_{13} & S_{23} & S_{33} & S_{34} & S_{35} & S_{36}\\S_{14} & S_{24} & S_{34} & S_{44} & S_{45} & S_{46}\\S_{15} & S_{25} & S_{35} & S_{45} & S_{55} & S_{56}\\S_{16} & S_{26} & S_{36} & S_{46} & S_{56} & S_{66}\end{bmatrix}\begin{bmatrix}\epsilon_{11}\\\epsilon_{22}\\\epsilon_{33}\\\epsilon_{12}\\\epsilon_{23}\\\epsilon_{13}\end{bmatrix} \tag{2.2}$$

where $S_{11} = s_{1111}$, $S_{12} = s_{1122}$, $S_{13} = s_{1133}$, $S_{14} = s_{1112}$, $S_{15} = s_{1113}$, $S_{16} = s_{1113}$, $S_{22} = s_{2222}$, $S_{23} = s_{2233}$, $S_{24} = s_{2212}$, , $S_{25} = s_{2223}$, $S_{26} = s_{2213}$, $S_{33} = s_{3333}$, $S_{34} = s_{3312}$, $S_{35} = s_{3323}$, $S_{36} = s_{3313}$, $S_{33} = s_{3333}$, $S_{44} = s_{1212}$, $S_{45} = s_{1223}$, $S_{46} = s_{1213}$, $S_{55} = s_{2323}$, $S_{56} = s_{2313}$ and $S_{66} = s_{1313}$.

In Eq2.2, the stiffness components S_{IJ} are written as symmetric. To show the symmetry of these components, consider the elastic strain energy stored in the body per unit volume given by:

$$W = \frac{1}{2}\sum_{I=1}^{6}\sigma_I\epsilon_I \tag{2.3}$$

Substituting Hooke's law, Eq2.2 in Eq2.3 , one obtains:

$$W=\frac{1}{2}\sum_{I=1}^{6}\sum_{J=1}^{6}S_{IJ}\epsilon_J\epsilon_I \tag{2.4}$$

Now, by partial differentiation of Eq2.4

$$\frac{\partial W}{\partial\epsilon_I\epsilon_J} = S_{IJ} \tag{2.5}$$

Because the differentiation does not necessarily need to be in either order,

$$S_{IJ} = S_{JI} \tag{2.6}$$

For the general anisotropic material there must be 36 constants of the stiffness matrix; this number reduces to 21 independent elastic constants because of the symmetries involved in the stiffness tensor components s_{ijkl}. The inverse of Eq2.1 may be expressed as

$$\epsilon_{ij} = c_{ijkl}\sigma_{kl} \tag{2.7}$$

where the c_{ijkl} are the components of the flexibility tensor. Because $c_{ijkl}=s_{ijkl}^{-1}$, the symmetries of s_{ijkl} carry over to c_{ijkl}.

For a lamina, in the plane perpendicular to the fibers the material may be approximately considered as isotropic. Such transversely isotropic materials have the compliance and stiffness matrices given in Voigt form respectively by

$$C = \begin{bmatrix} \frac{1}{E_t} & -\frac{\nu_t}{E_t} & -\frac{\nu_l}{E_t} & 0 & 0 & 0 \\ -\frac{\nu_t}{E_t} & \frac{1}{E_t} & -\frac{\nu_l}{E_t} & 0 & 0 & 0 \\ -\frac{\nu_l}{E_t} & -\frac{\nu_l}{E_t} & \frac{1}{E_l} & 0 & 0 & 0 \\ 0 & 0 & 0 & \frac{\nu_t+1}{E_t} & 0 & 0 \\ 0 & 0 & 0 & 0 & \frac{1}{2G_L} & 0 \\ 0 & 0 & 0 & 0 & 0 & \frac{1}{2G_L} \end{bmatrix} \tag{2.8}$$

and

$$S = \begin{bmatrix} \frac{E_lE_t\nu_l^2-E_t^2}{E_t\nu_t^2+2E_l\nu_l^2\nu_t+2E_l\nu_l^2-E_t} & -\frac{E_t^2\nu_t+E_lE_t\nu_l^2}{E_t\nu_t^2+2E_l\nu_l^2\nu_t+2E_l\nu_l^2-E_t} & -\frac{E_lE_t\nu_l}{E_t\nu_t+2E_l\nu_l^2-E_t} & 0 & 0 & 0 \\ -\frac{E_t^2\nu_t+E_lE_t\nu_l^2}{E_t\nu_t^2+2E_l\nu_l^2\nu_t+2E_l\nu_l^2-E_t} & \frac{E_lE_t\nu_l^2-E_t^2}{E_t\nu_t^2+2E_l\nu_l^2\nu_t+2E_l\nu_l^2-E_t} & -\frac{E_lE_t\nu_l}{E_t\nu_t+2E_l\nu_l^2-E_t} & 0 & 0 & 0 \\ -\frac{E_lE_t\nu_l}{E_t\nu_t+2E_l\nu_l^2-E_t} & -\frac{E_lE_t\nu_l}{E_t\nu_t+2E_l\nu_l^2-E_t} & \frac{E_lE_t\nu_t-E_lE_t}{E_t\nu_t+2E_l\nu_l^2-E_t} & 0 & 0 & 0 \\ 0 & 0 & 0 & \frac{E_t}{\nu_t+1} & 0 & 0 \\ 0 & 0 & 0 & 0 & 2G_L & 0 \\ 0 & 0 & 0 & 0 & 0 & 2G_L \end{bmatrix} \tag{2.9}$$

in which E_l and E_t are Young's moduli in the longitudinal and transverse directions; G_L is the out-of-plane shear modulus, ν_l is poisson ratio in the longitudinal direction and ν_t is poisson ratio in the transverse direction. In FRP laminates E_l, E_t , G_L and ν_t can simply be calculated using the Young's moduli for fiber and matrix and the volume fraction of fibers by using the rule of mixtures as follows:

$$f = \frac{V_f}{V_f + V_m} \tag{2.10}$$

$$E_l = fE_f + (1-f)E_m \tag{2.11}$$

$$E_t = \left(\frac{f}{E_f} + \frac{1-f}{E_m}\right)^{-1} \tag{2.12}$$

$$\nu_l = f\nu_f + (1-f)\nu_m \tag{2.13}$$

$$G_L = \left(\frac{f}{G_f} + \frac{1-f}{G_m}\right)^{-1} \tag{2.14}$$

where f is the volume fraction of the fibers, E_f is Young's modulus of the fibers, E_m is Young's modulus of the matrix, ν_f is the Poisson ratio of the fibers, ν_m is the Poisson ratio of the matrix, G_f is shear modulus of the fibers and G_m is shear modulus of the matrix.

2.4 Failure Modes in Unidirectional FRPs

The development of stress-strain boundaries for a microplane model is a challenging process. A good knowledge about the general 3D state of stress behavior of the material including the inelastic behavior, the material's response in different loading paths, directional properties, and fracture processes are needed. In what follows, the mechanical behavior of transversely isotropic FRPs is described.

2.4.1 Longitudinal Compressive Failure

The compressive loading of a unidirectional FRP has the most complex failure mechanisms. The compressive strength of the unidirectional FRPs is often less than 60% of their tensile strength, and usually, compressive failure is design limiting. Compression in fiber direction can cause difficulties in experimental and theoretical models because of the micro-buckling of fibers, longitudinal splitting of a column of fibers, kink-band propagation in the fibers, and shear failure of fibers.

2.4.2 Micro-buckling

This mode of failure is the dominant one in uniaxial compression in the longitudinal direction. In this mode, individual fibers buckle in the matrix anti-symmetrically (originally suggested by Rosen) which causes the compressive strength to drop [15]. Fig2.4 shows a typical micro-bucking phenomenon.

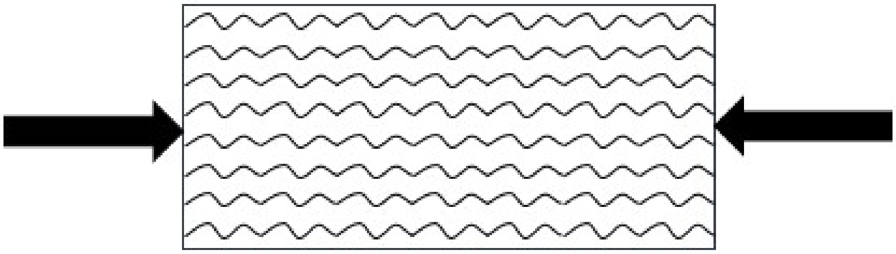

Figure 2.4: Micro-bucking

The compressive strength for this failure mode is given by

$$S_{LC} = \frac{G_m}{1 - V_f} \tag{2.15}$$

in which S_{LC}, G_m and V_f are longitudinal compressive strength, matrix shear modulus, and volume fiber fraction respectively. Experimental data shows that compressive strength from Eq3.5 is much higher than observations in real applications. Lower compressive strength can be predicted in conjunction with microbuckling if one considers imperfections in the form of initial curvature of the fiber or initial fiber misalignment [16]. In these models, the imperfections are assumed to be uniform. In actuality, fiber curvature and misalignment are likely to be rather random. However, these models are valuable in demonstrating the effect of these initial imperfections on compressive strength. Fiber microbuckling, as illustrated in Eq3.5, is not observed in practice as the primary failure mode.

2.4.3 Longitudinal Splitting

Current state-of-the-art matrix materials are stiff enough (at least at room temperature) to provide sufficient support for the fiber. If longitudinal splitting occurs first as shown in Fig2.5, however, the fiber loses support and can buckle as a column. Longitudinal splitting can be initiated by transverse stresses. Such transverse stresses can be induced even in compression loading of a unidirectional composite due to a mismatch of Poisson's ratios between the fiber and the matrix.

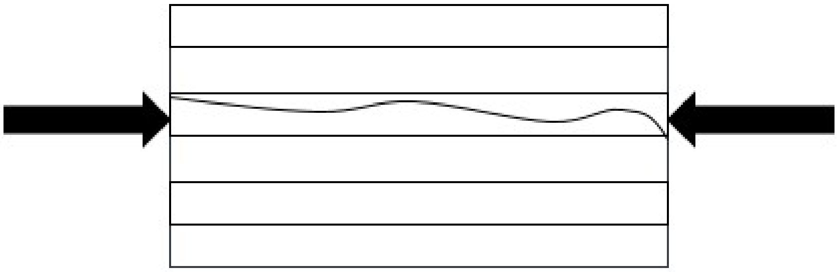

Figure 2.5: Longitudinal splitting

2.4.4 Kink-band

Another failure mode discussed in detail by Hahn and Williams [17] involves the local bending or buckling of a fiber. This local fiber instability can lead to the buckling of adjacent fibers and the formation of a ”kink-band,” leading to shear failure. A kink-band is illustrated in Fig2.6. The formation of kink-bands can be initiated in regions where there are voids or where the fiber-matrix interface strength is locally weakened.

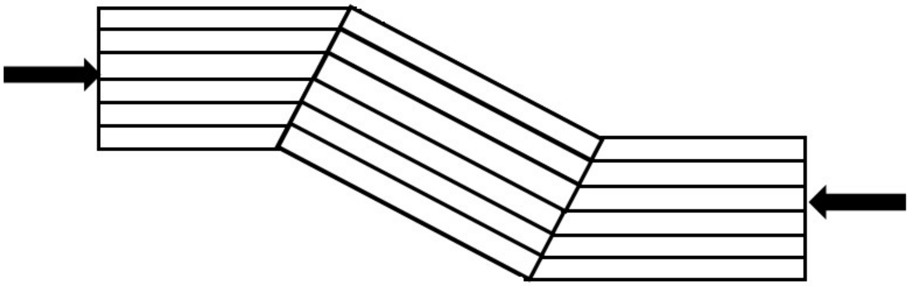

Figure 2.6: Kink-band

2.5 Shear Failure of Fibers

The final failure mode observed in a unidirectional composite under compression loading in the logitudinal direction is the shear failure of the fiber as shown in Fig2.7. This failure mode is commonly observed in pitch base graphite fiber composites and can also be produced in pan base graphite fiber composites.

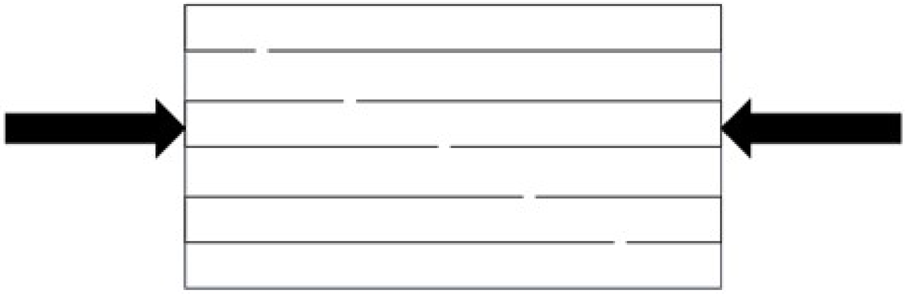

Figure 2.7: Shear failure of fibers

Furthermore, there are other failure modes like shear band formation and buckle delamination, which are less common. The problem in characterizing composite compression strength arises because these failure modes are all possible in longitudinal compression. Load introduction, free-edge effects, and specimen misalignment are factors that may influence the failure mode. In some cases, the observed failure mode is secondary to other events like delamination.

2.5.1 Longitudinal Tensile Failure

The tensile failure for longitudinal direction for unidirectional FRPs is better understood than compressive failure. Also, for multidirectional composites, usually, failure occurs when the 0° plies fail. In the fiber-reinforced composites, fibers in the bundle do not have the same strength. In the tension of unidirectional fiber-reinforced composites, the weakest fibers fail and stop carrying load upon increasing the tensile load. The released load from failed fibers are transferred to the neighboring fibers [18, 19, 20, 21]. The increasing load concentration on the neighbor fibers increases the probability of failure in these fibers. Eventually a high enough load concentration causes the development of fiber breakage in clusters, leading to more intensified stress concentration and finally fracture propagation through the whole cross section. Two key ingredients in the tensile failure of FRPs are stress redistribution around a broken fiber and the associated fiber strength statistics. Matrix properties and its interface with the fibers govern the stress redistribution. The strength of the fibers obey Weibull distribution ([22]). The standard Weibull probability distribution applicable to bundles of fiber failing in longitudinal tension is given by

$$p\left(\sigma_f\right) = 1 - exp\left(-\left(\frac{L}{L_0}\right)\left(\frac{\sigma_f}{\sigma_0}\right)^m\right) \tag{2.16}$$

where p is the probability density of failure, L is the characteristic gauge length, L_0 is the reference gauge length, σ_f is the fiber strength, σ_0 is the scale parameter and m is the Weibull modulus.

2.5.2 Lateral Failure

Experimental data show that the dominant modes of the lateral direction failure in the unidirectional FRPs are failure of the matrix and interfacial fiber-matrix debonding [23]. The failure of the matrix can occur by yield in the matrix and by cavitation-induced brittle matrix failure. Fiber-matrix debonding depends on the surface treatments of the fibers, the inherent chemical properties of matrix and fibers, and the manufacturing process of the FRPs [24, 25, 26].

2.6 Models for the Mechanical Behavior of FRPs

Plenty of models exist for predicting the mechanical behavior of FRPs. In most models, the prediction of strength is the main goal. For example in [27], a model for tensile loading in the longitudinal direction is presented. This model takes into account the statistical distribution of the flaws and imperfections among fibers. However, the stresses in the matrix are neglected by the argument that they are relatively small compared to those in the fibers. Similarly, the fiber shear strains are ignored by the argument that the shear strains in the matrix are higher. Efforts are made to model the FRP mechanical behavior in compression in the longitudinal direction in [28, 29]. In [30], a model for lateral loading in FRPs is presented. It considers interface decohesion and matrix plastic deformations. Shear strength prediction based on local stress distributions is treated in the model studied in [31]. Tsai-Wu failure criterion [32] is focused on the strength of FRPs subjected to multiaxial loading. More recently, a model has been developed for anisotropic damage in FRPs in [33]. In this model, the aim is the prediction of failure and post-failure. However, the experimental data consists of a single strength value.

A micromechanical model for the unidirectional FRP laminates is proposed in [34]. One shortcoming of this study is that the predicted FRP behavior is compared only with the shear-compression failure envelope. Also, predicted crack patterns are not compared with the experimentally observed crack patterns. Another disadvantage of this model is the explicit modelling of fiber-matrix interfaces, which makes the model unsuitable for large scale finite element analysis in complex structures such as ship masts and aircraft wings. Ideally a transition from microscale FRP behavior to macroscale FRP behavior is desired so that large scale finite element analyses of large structure for optimum design purposes becomes feasible. Another micromechanics based model is the one proposed in [35]. This model includes a non-iterative element-failure method integrated with a micromechanics-based failure criterion. However, the validation of model predictions by optimally fitting experimental data is scant and limited to only four strength points in 3 different failure envelopes.

In [36], a micromechanical smeared-crack model for FRPs is developed. The model considers neither compression and shear behaviors, nor strength envelopes. Furthermore, the validation includes only comparison with experimental data obtained from uniaxial tension of notched specimens. In [37], another micromechanical model for the plasticity of FRPs is proposed. There is no comparison to the experimental data in this study. The compressive strength of composite plates with a hole is studied in

[38], but the comparison of the model predictions to experimental data is limited to the qualitative crack patterns and six strength points. None of these models have the verified capability to predict and simulate the mechanical behavior of FRPs in general three-dimensional states of stress. Furthermore, none of these models are suitable for large scale finite element analyses of large structures needed in space and automotive industries. This study presents a new model based on the microplane concept for transversely isotropic FPRs: It not only treats the arbitrary three-dimensional stress states but also it is suitable for large scale finite element analyses of large structures with complex geometries.

2.7 Microplane Model

The idea of the Microplane model originates from G. I. Taylor in 1938 [39]. Based on this study, the slip theory of plasticity is developed by Batdorf and Budiansky [40]. Later, a series of reliable models based on the same slip theory of plasticity, called the Taylor models, are developed for plastic-hardening of polycrystalline metals [41, 42, 43, 44]. In the slip theory of plasticity, the stress vectors are calculated by the so-called “static constraint”. It means that the slip plane constitutive laws depend on the slip plane stresses obtained by projecting the Cauchy stress tensor onto the slip planes. The plastic strains are calculated taking into account work hardening on each slip plane using these traction vectors. Strain vectors then are superposed to yield the continuum plastic strain tensor. Elastic strain tensor is obtained using the elastic stiffness tensor and the Cauchy stress tensor. Finally, this plastic strain tensor is added to the elastic strain tensor to complete the elastoplastic Taylor type slip plane model.

The microplane models extend the Taylor type plastic slip plane models to multiple material behaviors such as elasticity, plasticity, fracture and damage. The very first microplane model is presented for constitutive modelling of elasticity, plasticity and fracture of concrete. The term microplane refers to a generic plane on which mechanical processes characteristic of the material take place. For an isotropic material with weak fracture and damage induced anisotropy, these planes of interest must discretize all directions in 3D. The FRPs are quasi-brittle materials similar to concrete [45, 46] but they are strongly anisotropic. Obviously, the static constraint used in the slip theory of plasticity cannot model the entire range of fracture and damage [43] in quasibrittle materials. To model the entire range of fracture and damage, the so-called "kinematic constraint" must be used. It means that the microplane strains are obtained from the projection of the strain tensor onto the microplanes, and the microplane constitutive laws are defined as functions of these microplane strain vectors. Thus, in the microplane models, the material behavior is defined as relations between the components of microplane stress and strain vectors.

By contrast, in the classical approach of tensorial models, the constitutive laws must be constructed in terms of the invariants of stress and strain tensors and their principal values. For example, in tensorial models, a relation between the second invariant of the deviatoric stress tensor J_2 and the first invariant of the stress tensor I_1 is needed to model internal friction in an average sense in concrete and other similar geomaterials. In reality, however, the internal friction is the result of frictional slip occurring on specific planes, which the microplane approach can easily model without using any of these invariants.

The static and kinematic constraints can hold simultaneously for a material only in the elastic range of the mechanical behavior. For softening behavior of quasi-brittle materials because of localized fracture, the kinematic constraint is needed [47, 48]. The microplane stress vectors calculated using the elastoplastic fracturing constitutive laws as functions of the microplane strains are integrated over the surface of hemisphere using the principle of virtual work to yield the macroscopic stress tensor. Microplane models for concrete using kinematic constraint have been developed and improved since 1980. Notable models range from the model M1 through the model M7, in each model a wider range of mechanical behavior of concrete being addressed. Microplane models are developed for other materials such as anisotropic rock called shale[49], unidirectional FPRs [14, 50], anisotropic braided FRP composites [51, 52], and biological soft tissue [53, 54]. Among the microplane models for concrete, the model M7 performs best by solving of the problems exhibited by earlier versions such as excessive lateral expansion in compression, excessive lateral contraction in tension, stress locking in far post-peak uniaxial tension as well as unrealistic unloading and reloading in tension. In addition, the model M7 retained all other predictive capabilities of its predecessors under a wide variety of states of stress [47, 49, 55, 56].

Chapter 3

Cylindrical Microplane Model

The microplane models for isotropic materials with weak, fracture induced anisotropy are based on the spherical geometry, e.g. microplane models M0 through M7 and microplane models for soft tissue. Figure 3.1 shows the discretization of all directions in 3D space using Gaussian quadrature for isotropic materials with weak fracture induced anisotropy.

The main difference in the case of FRPs is the presence of a strong anisotropy due to the enormous difference in the stiffness and strength in different directions exhibited by the material. Although in this case a spherical geometry is clearly not helpful to capture the material behavior, a microplane model for FRPs using a spherical geometry has already been proposed. This model, which was proposed in 2008, is called the spectral stiffness microplane model. It relies on the spectral decomposition of the stiffness tensor over a spherical geometry [14, 50]. The problem with this method is that the model loses its intuitive nature and restricts the data fitting capabilities of the model. Essentially this model has similar difficulties as tensorial models and thus it does not contribute to a detailed modeling of all aspects of the mechanical behavior of the material. Cylindrical geometry is the natural choice for the modelling of the

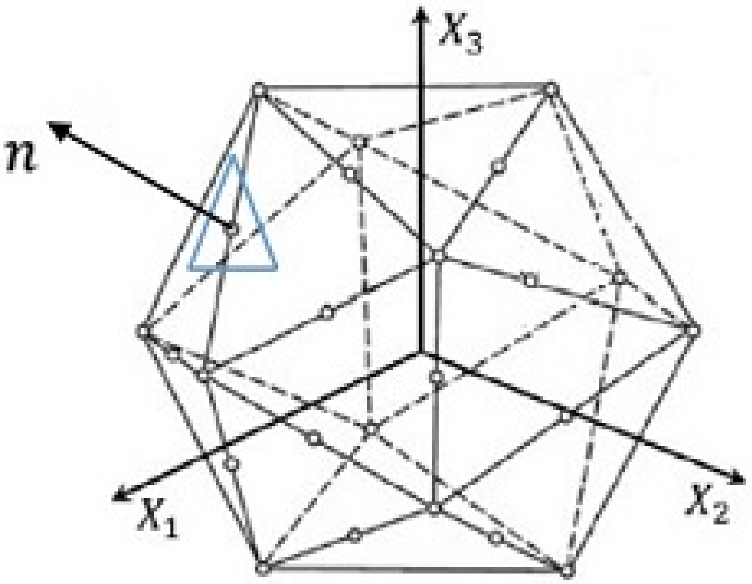

Figure 3.1: Spherical microplane model discretization using Gaussian quadrature , taken from [47].

mechanical behavior of transversely isotropic FRPs. The cylinder, with side and top microplanes, naturally represents both the fiber and the matrix by directionally uncoupling the respective mechanical behaviors. In figure 3.2 the cylindrical microplanes are shown.

3.1 Microplane Stress-Strain Boundaries

The kinematic constraint implies that microplane stress vectors must be functions of microplane strains due to the strain-softening of the FRPs. These constitutive laws are defined as bounds, or strain-dependent yield surfaces, on the microplane stresses. The microplane stress-strain boundaries dictate the material behavior as elastic when the

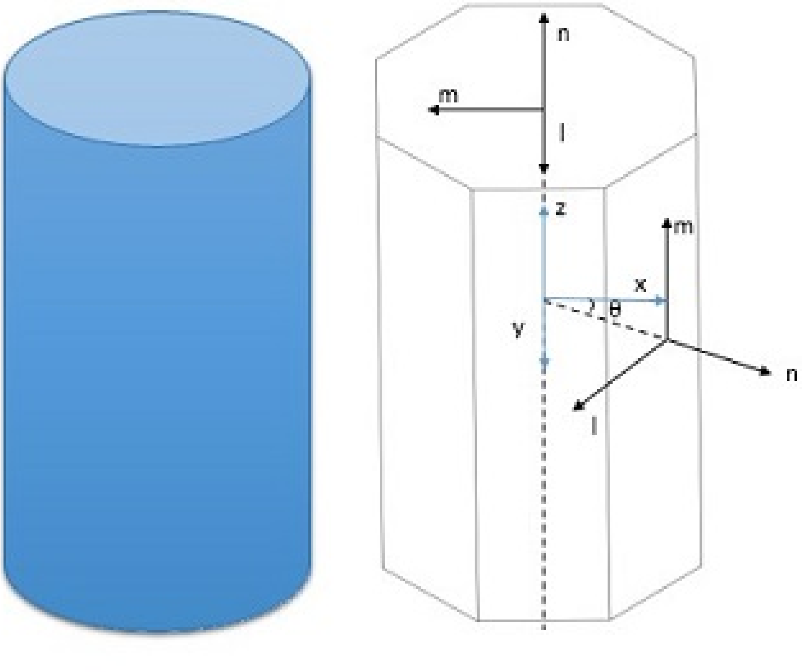

Figure 3.2: The cylindrical microplanes

boundaries are not exceeded. Inelastic fracturing behavior is simulated by the boundaries when the elastic microplane stresses exceed the boundaries causing the stresses to drop vertically to the boundary at the same strain.

The concept of boundaries is illustrated in Figure3.3, which depicts the evolution of microplane stress with increasing microplane strains. Consider a state of stress in which on a given microplane, stress and strain are given by σ_0 and ϵ_0. If an increment of $\Delta\epsilon$ is applied on the strain acting on this microplane, using elasticity, the value of the stress becomes $\sigma_{Elastic}$, but because this stress exceeds the boundary, the inelastic stress is calculated by a vertical drop to the boundary as σ_{Final}.

In order to obtain the boundaries for the cylindrical microplane model for transversely isotropic FRPs, the stress-strain boundaries for the existing microplane models

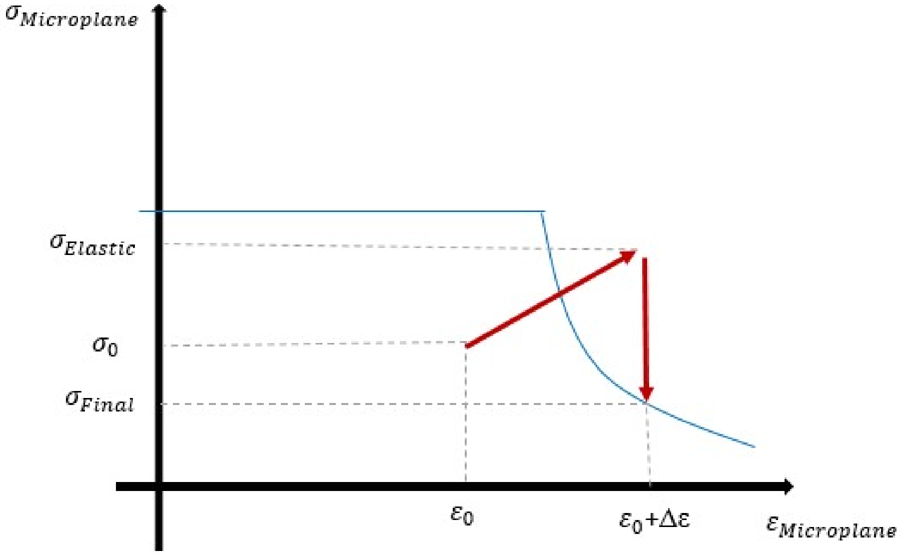

Figure 3.3: Microplane stress-strain boundary

is to be reviewed. The concept of the boundaries to characterize all inelastic behavior for concrete is introduced in the model M3 [57]. In the models M1 and M2, a smoothly curved inelastic stress-strain relation is used on the microplane [58, 59]. The difficulty with this approach is the calibration of the model: It turns out that it is difficult to control the peak stress and post-peak strain softening behavior. In model M3, the sudden transition from elastic behavior inside the boundary to softening on the boundary creates a very sharp macroscopic response compared to test data. In model M2, separate strain softening for volumetric and deviatoric stress components are implemented. This separation is justified postulating two independent softening processes that occur simultaneously. Strain softening is expected to localize into one of these stress components [60]. Indeed, strain localizes into the volumetric softening while the deviatoric stress is unloaded. Consequently, excessive lateral expansion happens in compression.

By the introduction of stress-strain boundary in model M3, the tensile strain-softening is controlled through a boundary on the microplane normal stress component as in the model M1. The normal stress boundary is imposed in addition to deviatoric boundaries, and the problem of excessive lateral expansion in M2 is corrected. In model M4, horizontal boundaries (yield limits) are introduced to account for pressure dependent plasticity of concrete [61]. Furthermore, these horizontal yield limits prevent localization of inelastic strains to just one microplane while the rest of the microplanes unload in the strain-softening regime of the mechanical behavior. With the introduction of horizontal boundaries, the yielding gradually spreads over many microplanes. The disadvantages of the M4 model are (1) spurious excessive lateral contraction in tension and (2) stress locking at far post-peak tensile strains. In model M5, this problem is tackled by employing two isotropic microplane models statically and kinematically constrained and coupled in series. However, the robustness emerged as a new difficulty in model M5 preventing its use in the finite element analysis in arbitrary 3D states of stress. In the model M5, the shear boundary has different roles in tension and in compression. In compressive loading, the shear boundary serves as a frictional yield surface in the plane of shear stress versus normal stress, with the cohesion gradually approaching zero as the fracturing damage increases. However, in the tensile range, the frictional boundary cannot be closed, because it would cause excessive pre-peak plastic strain and shift the stress peak too far to the right along the strain axis. Rather, the shear response in tension must remain almost elastic until the peak, which is ensured by elevating the tensile portion of the frictional boundary. Thus, the frictional boundary is formulated as shear stress boundary proportional to the normal tensile stress in tension.

In the microplane model M7, the lastest microplane model for concrete, there is no tensile deviatoric boundary unlike the models M3 through M6. Thus, there are only four different stress-strain boundaries in the model M7:

1. Normal boundary, which defines tensile normal stress as a function of tensile normal strain.

2. Volumetric boundary, which defines pressure as a function of volumetric strain.

3. Deviatoric boundary, which defines compressive deviatoric stress as a function of compressive deviatoric strain.

4. Plastic-frictional yield surface, which defines shear stress resultant as a function of normal stress.

In the models M4 and M5, the shear boundary (the plastic-frictional yield surface) is applied to shear components in **m** and **l** directions separately. On the other hand, it is applied to the shear resultant in the model M7 instead of shear components. The resultants of the microplane stress σ_T and strain ϵ_T are defined as:

$$\epsilon_T = \sqrt{\epsilon_L^2 + \epsilon_M^2} \text{ and } \sigma_T = \sqrt{\sigma_L^2 + \sigma_M^2} \tag{3.1}$$

The spherocylindrical microplane constitutive model, developed for shale [62, 63] and other anisotropic rocks, is made up of a cylindrical microplane model and a classical spherical microplane model. The classical spherical and the cylindrical microplane models are coupled in parallel. The kinematic constraint is used in both models. The tensile normal boundary of the spherical part is used to simulate the tensile fracture and cracking damage. The tensile deviatoric boundary of the spherical part is introduced to control the lateral strain with volume expansion under weakly confined or unconfined compression. The compressive deviatoric boundary of the spherical system controls the spherical part axial crushing strain in compression when the lateral confinement is too weak. The shear boundary of the spherical part, which is a frictional shear boundary, depends on normal microplane stress, microplane orientation (dip angle), and volumetric strain. The compressive volumetric boundary of the spherical part is designed so that the hydrostatic compression in quasibrittle materials like concrete and shale creates no softening. Also, pressure closes microcracks and voids causing progressive hardening. The tensile normal boundary of the cylindrical part controls the tensile cracking. The compressive normal boundary of the cylindrical part controls the failure mechanism in compression when the confining pressure is not too high. The shear boundary of the cylindrical part mainly controls the failure when the confining pressure is high.

3.2 Cylindrical Microplane Formulation

In the cylindrical microplane model the elastic stress and strain vectors for each microplane are obtained by applying the static constraint and the inelastic strains are obtained by applying the kinematic constraint [44]:

$$\epsilon_N = \epsilon_{ij} N_{ij}; \quad \epsilon_M = \epsilon_{ij} M_{ij}; \quad \epsilon_L = \epsilon_{ij} L_{ij} \tag{3.2}$$

$$\sigma_N^e = \sigma_{ij}^e N_{ij}; \quad \sigma_M^e = \sigma_{ij}^e M_{ij}; \quad \sigma_L^e = \sigma_{ij}^e L_{ij} \tag{3.3}$$

In Eq3.2 and 3.3 , ϵ_N is the normal microplane strain, ϵ_L and ϵ_M are the components of the in-plane microplane shear strain vector, σ_N^e is the elastic microplane normal stress, σ_L^e and σ_M^e are the in-plane microplane shear stress vector components, N_{ij} , M_{ij} and L_{ij} are geometric tensors defined by

$$N_{ij} = n_i n_j; \quad M_{ij} = \tfrac{1}{2}\left(n_i m_j + n_j m_i\right); \quad L_{ij} = \frac{1}{2}\left(n_i l_j + n_j l_i\right) \tag{3.4}$$

where $i, j = 1, 2, 3$.

In Eqs3.4, $\mathbf{n}$ is the unit normal vector defined at each microplane, $\mathbf{m}$ and $\mathbf{l}$ are orthogonal in-plane unit vectors in each microplane. For lateral microplanes these vectors are given by

$$\mathbf{n} = [\cos\theta \;\; \sin\theta \; 0]\,; \quad \mathbf{m} = [0\;0\;1]\,; \mathbf{l} = [-\sin\theta \;\; \cos\theta \; 0] \tag{3.5}$$

Thus

$$\mathbf{N} = \begin{bmatrix} \cos^2\theta & \cos\theta\sin\theta & 0 \\ \cos\theta\sin\theta & \sin^2\theta & 0 \\ 0 & 0 & 0 \end{bmatrix}$$

$$\mathbf{L} = \begin{bmatrix} -\cos\theta\sin\theta & (\cos^2\theta - \sin^2\theta)/2 & 0 \\ (\cos^2\theta - \sin^2\theta)/2 & \cos\theta\sin\theta & 0 \\ 0 & 0 & 0 \end{bmatrix} \tag{3.6}$$

$$\mathbf{M} = \begin{bmatrix} 0 & 0 & (\cos\theta)/2 \\ 0 & 0 & (\sin\theta)/2 \\ (\cos\theta)/2 & (\sin\theta)/2 & 0 \end{bmatrix}$$

For the top microplane these vectors are given by:

$$\mathbf{n} = [0\;0\;1]\,; \quad \mathbf{m} = [-1\;0\;0]\,; \quad \mathbf{l} = [0\;1\;0] \tag{3.7}$$

which lead to

$$
\mathbf{N}^t = \begin{bmatrix} 0 & 0 & 0 \\ 0 & 0 & 0 \\ 0 & 0 & 1 \end{bmatrix}
$$

$$
\mathbf{M}^t = \begin{bmatrix} 0 & 0 & -1/2 \\ 0 & 0 & 0 \\ -1/2 & 0 & 0 \end{bmatrix} \tag{3.8}
$$

$$
\mathbf{L}^t = \begin{bmatrix} 0 & 0 & 0 \\ 0 & 0 & 1/2 \\ 0 & 1/2 & 0 \end{bmatrix}
$$

3.3 Micro-macro Stress Equilibrium

Consider a unit cylinder with radius r = 1 and unit height h = 1. The virtual work of stress and strain tensors over the volume of this cylinder is given by $\int_{\Omega} \sigma_{ij}\delta\epsilon_{ij}\mathrm{d}\Omega$. The virtual work of the microplane stress and strain components over the surface of this unit cylinder is given by $\int_{\partial\Omega} (\sigma_N\delta\epsilon_N + \sigma_M\delta\epsilon_M + \sigma_L\delta\epsilon_L)\,\mathrm{d}A$. Next, we postulated that

$$
\int_{\mathrm{V}} \sigma_{\mathrm{ij}}\delta\epsilon_{\mathrm{ij}}\mathrm{dV} = \int_{\mathrm{A}} (\sigma_{\mathrm{N}}\delta\epsilon_{\mathrm{N}}+\sigma_{\mathrm{M}}\delta\epsilon_{\mathrm{M}}+\sigma_{\mathrm{L}}\delta\epsilon_{\mathrm{L}})\,\mathrm{dA} \tag{3.9}
$$

For fracturing materials, the relationship between the strain tensor components ϵ_{ij} and the microplane strains ϵ_N, ϵ_M and ϵ_L is given by Eq3.2. Taking the variation relative to the strain tensor components ϵ_{ij} of Eq3.2 and substituting it into Eq3.9 leads to the micro-macro stress equilibrium equation given by

$$
\left[\sigma_{\mathrm{ij}} \int_{\mathrm{V}} \mathrm{dV} - \int_{\mathrm{A}} \left(\sigma_{\mathrm{N}}\mathrm{N}_{\mathrm{ij}} + \sigma_{\mathrm{M}}\mathrm{M}_{\mathrm{ij}} + \sigma_{\mathrm{L}}\mathrm{L}_{\mathrm{ij}}\right)\mathrm{dA}\right]\delta\epsilon_{\mathrm{ij}} = 0
$$

$$\forall \;\; \delta\epsilon_{\mathrm{ij}} \neq 0$$

which leads to

$$\sigma_{\mathrm{ij}} = \frac{2}{\pi}\int_{\mathrm{A}} \left(\sigma_{\mathrm{N}}\mathrm{N}_{\mathrm{ij}} + \sigma_{\mathrm{M}}\mathrm{M}_{\mathrm{ij}} + \sigma_{\mathrm{L}}\mathrm{L}_{\mathrm{ij}}\right)\, dA \tag{3.10}$$

In numerical calculations, the integral in Eq3.10 is approximated by Gaussian quadrature using

$$\sigma_{\mathrm{ij}} = \frac{2}{\pi}\sum_{k=1}^{np} w_k \left(\sigma_{\mathrm{N}}\mathrm{N}_{\mathrm{ij}} + \sigma_{\mathrm{M}}\mathrm{M}_{\mathrm{ij}} + \sigma_{\mathrm{L}}\mathrm{L}_{\mathrm{ij}}\right) \tag{3.11}$$

where w_k are the Gaussian quadrature weights and the expression in the parenthesis is evaluated at Gaussian quadrature points. For the half cylinder, $\sum_{k=1}^{np} w_k = \pi + \pi = 2\pi$ in which the first π comes from side microplanes and the second one comes from the top microplanes. At the top of the cylinder, there is only one microplane and consequently, the weight factor is equal to the area of the circle at the top, and its value is π. However, for the top microplane the area is considered as $\pi/2$ so as to match the stress tensor calculated using the transversely isotropic elastic stiffness tensor. Thus, if top microplane is considered separately one has

$$\sigma_{\mathrm{ij}} = \frac{2}{\pi}\left[\int_{\mathrm{A}} (\sigma_{\mathrm{N}}\mathrm{N}_{\mathrm{ij}} + \sigma_{\mathrm{M}}\mathrm{M}_{\mathrm{ij}} + \sigma_{\mathrm{L}}\mathrm{L}_{\mathrm{ij}})\,\mathrm{dA} + \int_{A_t} (\sigma_{\mathrm{Nt}}\mathrm{N}_{\mathrm{ij}} + \sigma_{\mathrm{Mt}}\mathrm{M}_{\mathrm{ij}} + \sigma_{\mathrm{Lt}}\mathrm{L}_{\mathrm{ij}})\,\mathrm{d}A_t\right] \tag{3.12}$$

which leads to

$$\sigma_{\mathrm{ij}} = \frac{2}{\pi}\left[\sum_{k=1}^{np-1} w_k(\sigma_{\mathrm{N}}\mathrm{N}_{\mathrm{ij}} + \sigma_{\mathrm{M}}\mathrm{M}_{\mathrm{ij}} + \sigma_{\mathrm{L}}\mathrm{L}_{\mathrm{ij}})\right] + 2(\sigma_{\mathrm{Nt}}\mathrm{N}_{\mathrm{ij}} + \sigma_{\mathrm{Mt}}\mathrm{M}_{\mathrm{ij}} + \sigma_{\mathrm{Lt}}\mathrm{L}_{\mathrm{ij}}) \tag{3.13}$$

where σ_{Nt} , σ_{Mt} and σ_{Lt} are the microplane normal, **m** direction shear and **l** direction shear stresses respectively for the top plane.

3.4 Weight Factors

Theoretically when the number of microplanes (which coincides with the number of quadrature points) increases, the accuracy also must increase. However, there is an optimum number of microplanes that provides sufficiently high accuracy and thus using more microplanes yields only diminishing improvement in the accuracy at an increasing computational cost. In order to use the Gaussian quadrature the first integral in Eq.3.12 for the lateral microplanes can be written as

$$\int_{\mathrm{A}} (\sigma_{\mathrm{N}}\mathrm{N}_{\mathrm{ij}}+ \sigma_{\mathrm{M}}\mathrm{M}_{\mathrm{ij}}+\sigma_{\mathrm{L}}\mathrm{L}_{\mathrm{ij}})\ \mathrm{dA} = \frac{1}{2}\int_{0}^{2\pi} (\sigma_{\mathrm{N}}\mathrm{N}_{\mathrm{ij}}+ \sigma_{\mathrm{M}}\mathrm{M}_{\mathrm{ij}}+\sigma_{\mathrm{L}}\mathrm{L}_{\mathrm{ij}}) d\theta \tag{3.14}$$

Using the transformation a = $\theta/\pi - 1$ the right hand side of Eq3.14 becomes

$$\frac{1}{2}\int_{0}^{2\pi} (\sigma_{\mathrm{N}}\mathrm{N}_{\mathrm{ij}}+ \sigma_{\mathrm{M}}\mathrm{M}_{\mathrm{ij}}+\sigma_{\mathrm{L}}\mathrm{L}_{\mathrm{ij}}) d\theta = \frac{\pi}{2}\int_{-1}^{1} (\sigma_{\mathrm{N}}\mathrm{N}_{\mathrm{ij}}+ \sigma_{\mathrm{M}}\mathrm{M}_{\mathrm{ij}}+\sigma_{\mathrm{L}}\mathrm{L}_{\mathrm{ij}}) da \tag{3.15}$$

From [64] one has

$$\int_{-1}^{1} f\,(\mathrm{x})\,d\mathrm{x} = \sum_{i=0}^{n} w_i.f(x_i) \tag{3.16}$$

For Gauss points numbers $n = 8, 16$ and 24 the linear locations and weights as well as the angular locations and weights are shown in Table3.1, Table3.2 and Table3.3 respectively in order to carry out the sum in Eq3.16.

i (Number of Microplane)	$\mathbf{x_i}$	$\mathbf{w_i}$	**θ(rad)**	$\mathbf{w_\theta}$
1	0.960289	0.101228	6.15843	0.159009
2	-0.96029	0.101228	0.124756	0.159009
3	0.796666	0.222381	5.644393	0.349315
4	-0.79667	0.222381	0.638793	0.349315
5	0.525532	0.313707	4.7926	0.492769
6	-0.52553	0.313707	1.490585	0.492769
7	0.183434	0.362684	3.717868	0.569702
8	-0.18343	0.362684	2.565318	0.569702

Table 3.1: Gauss points and the corresponding weights for 8 lateral microplanes

i (Number of Microplane)	$\mathbf{x_i}$	$\mathbf{w_i}$	**θ(rad)**	$\mathbf{w_\theta}$
1	0.9894	0.027152	6.249884	0.04265
2	-0.9894	0.027152	0.033301	0.04265
3	0.944575	0.062253	6.109063	0.097787
4	-0.94458	0.062253	0.174123	0.097787
5	0.865631	0.095159	5.861053	0.149475
6	-0.86563	0.095159	0.422133	0.149475
7	0.7554	0.12462	5.514752	0.195753
8	-0.7554	0.12462	0.768434	0.195753
9	0.617876	0.149595	5.082707	0.234983
10	-0.61788	0.149595	1.200478	0.234983
11	0.458016	0.169156	4.580492	0.26571
12	-0.45802	0.169156	1.702693	0.26571
13	0.2816	0.182603	4.026265	0.286832

14	-0.2816	0.182603	2.25692	0.286832
15	0.095	0.18945	3.440044	0.297587
16	-0.095	0.18945	2.843141	0.297587

Table 3.2: Gauss points and the corresponding weights for 16 lateral microplanes

i (Number of Microplane)	$\mathbf{x_i}$	$\mathbf{w_i}$	θ**(rad)**	$\mathbf{w}_\theta$
1	0.06405	0.127938	3.342812	0.200965
2	-0.06405	0.127938	2.940374	0.200965
3	0.19111	0.125837	3.741982	0.197665
4	-0.19111	0.125837	2.541203	0.197665
5	0.31504	0.12167	4.13132	0.19112
6	-0.31504	0.12167	2.151865	0.19112
7	0.43379	0.115506	4.504384	0.181436
8	-0.43379	0.115506	1.778801	0.181436
9	0.54549	0.107444	4.8553	0.168773
10	-0.54542	0.107444	1.428105	0.168773
11	0.64809	0.097619	5.177627	0.153339
12	-0.64809	0.097619	1.105558	0.153339
13	0.74012	0.08619	5.466748	0.135387
14	-0.74012	0.08619	0.816437	0.135387
15	0.82	0.073346	5.717699	0.115212
16	-0.82	0.073346	0.565487	0.115212
17	0.88641	0.059299	5.926332	0.093146
18	-0.88641	0.059299	0.356854	0.093146

19	0.93827	0.044277	6.089255	0.069551
20	-0.93827	0.044277	0.193931	0.069551
21	0.97472	0.028531	6.203766	0.044817
22	-0.97472	0.028531	0.079419	0.044817
23	0.99518	0.012341	6.268043	0.019386
24	-0.99518	0.012341	0.015142	0.019386

Table 3.3: Gauss points and the corresponding weights for 24 lateral microplanes

Chapter 4

Cylindrical Microplane Model in Finite Element Calculations

4.1 Development of the Stress- Strain Boundaries for Finite Element Calculations

During the development of the cylindrical microplane stress-strain boundaries, the initial shape of all the boundaries has been considered the same as in Fig3.3. The final form of these boundaries has been determined iteratively by successively solving the problems revealed by optimal data fitting of experimental data in each set of boundaries. Once all test data can be fit well, the iterations are stopped and the current microplane boundaries are accepted as the true boundaries.

In these iterative processes initially a single Gauss point driver is used to check the material responses to different load paths and correct the microplane boundaries accordingly. The driver is a small implicit program written in Fortran 90 that uses the initial stiffness method. Eventually the final form of these boundaries are calibrated and verified using finite element analyses. This intermediate step seems to accelerate the model development in its initial stages.

In what follows a total of 3 major iterations in obtaining the final form of the microplane boundaries are presented.

4.1.1 Iteration 1

The very first set of boundaries considered is as follows. For the normal boundary of the lateral microplanes, the following equations are considered for compression and tension respectively:

$$\sigma^B_{Ntm} = C_1 E_t \, e^{-(C_3 < \epsilon_N - k_1 >)} \tag{4.1}$$

$$\sigma^B_{Ncm} = C_2 E_t \, e^{-(C_4 < |\epsilon_N| - k_2 >)} \tag{4.2}$$

in which $< x >= \max(0, x)$ called the Macauley brackets; C_1, C_2, C_3, C_4, k_1 and k_2 are adjustable parameters.

The normal boundaries in tension and compression respectively for the top microplane are proposed as

$$\sigma^B_{Ntf} = C_5 E_l \, e^{-(C_7 < \epsilon_N - k_3 >)} \tag{4.3}$$

$$\sigma^B_{Ncf} = C_6 E_l \, e^{-(C_8 < |\epsilon_N| - k_4 >)} \tag{4.4}$$

where C_5,C_6, C_7, C_8, and k_4 are adjustable parameters.

The lateral microplane L and M-direction shear boundaries respectively are proposed to be

$$\sigma^B_{Lf} = \frac{C_9 \, (1+\nu_t)}{E_t} e^{-(C_{11} < |\epsilon_L| - k_5 >)} \tag{4.5}$$

$$\sigma^B_{Mm} = 2 C_{10} G_L \, e^{-(C_{12} < |\epsilon_M| - k_6 >)} \tag{4.6}$$

where C_9, C_{10}, C_{11}, C_{12}, k_5 and k_6 are adjustable parameters.

The top microplane L and M-direction shear behaviors must be described by the same boundary, which is given by

$$\sigma^B_{L,Mf} = 2C_{13}G_L \; e^{-(C_{14}<|\epsilon_L,M| \, - \, k_7>)} \tag{4.7}$$

in which C_{13}, C_{14} and k_7 are adjustable parameters. The parameters $C_1,\ C_2,\ C_5,\ C_6,\ C_9,\ C_{10},\ and\, C_{13}$ scale the stress-strain boundaries vertically. The parameters $k_1,\, k_2,\, k_3,\, k_4,\ k_5,\, k_6\ and\ k_7$ determine the initiation of softening in these boundaries. Finally the parameters $C_3,\ C_4,\ C_7,\ C_8,\ C_{11},\ C_{12}\ and\ C_{14}$ tune the post-peak slope of the stress-strain boundaries.

These boundaries unfortunately could not satisfactorily fit experimental data because the parameters cannot control the threshold of nonlinearity and the slope of the softening part of the response for lateral direction load paths.

4.1.2 Iteration 2

The next set of boundaries considered are as follows. The lateral microplane normal boundaries in compression and tension respectively are given by

$$\sigma^B_{Ntm} = c_1E_t(h_1\epsilon_N + s_1)e^{-(c_3<\epsilon_N - k_1>)} \tag{4.8}$$

$$\sigma^B_{Ntm} = c_2E_t(h_2\epsilon_N + s_2)e^{-(c_4<|\epsilon_N| - k_2>)} \tag{4.9}$$

where C_1,C_2, C_3, C_4, $h_1,\ h_2,\ S_1, S_2,\ k_1$ and $k_2$are adjustable parameters.

The normal microplane boundaries in tension and compression respectively for the top microplane are proposed as

$$\sigma^B_{Ntf} = E_l\,(h_3\epsilon_N + \ S_3)\ e^{-(C_5< \, \epsilon_N - \, k_3>)} \tag{4.10}$$

$$\sigma^{B}_{Ncf} = E_l\,(h_4\,|\epsilon_N| + S_4)\;e^{-(C_6<|\epsilon_N| - k_4>)} \tag{4.11}$$

where C_5,C_6, h_3, h_4, S_3, S_4, k_3 and k_4 are adjustable parameters.

The lateral microplane L and M-direction shear boundaries are given by

$$\sigma^{B}_{Lf} = \frac{E_t}{1+\nu_t}\,(h_5\,|\epsilon_L| + S_5)\;e^{-(C_7<|\epsilon_L| - k_5>)} \tag{4.12}$$

$$\sigma^{B}_{Mm} = 2G_L\,(h_6\,|\epsilon_M| + S_6)\;e^{-(C_8<|\epsilon_M| - k_6>)} \tag{4.13}$$

where C_7,C_8, h_5, h_6, S_5, S_6, k_5 and k_6 are adjustable parameters.

The L and M-direction shear boundaries respectively for the top microplane are given by

$$\sigma^{B}_{Lf} = 2G_L\,(h_7\,|\epsilon_L| + S_7)\;e^{-(C_9<|\epsilon_L| - k_7>)} \tag{4.14}$$

$$\sigma^{B}_{Mf} = 2G_L\,(h_7\,|\epsilon_M| + S_7)\,e^{-(C_9<|\epsilon_M| - k_7>)} \tag{4.15}$$

where C_9, S_7, h_7 and k_7 are adjustable parameters.

In this set of boundaries, the k-parameters can determine the fracture initiation point, S parameters tune the trigger point of nonlinearity, h-parameters determine nonlinear hardening slope and C-parameters determine the post-peak slope with the exception of C_1 and C_2, which tune the magnitude of the horizontal plastic response in the above boundaries. Thus these boundaries can be controlled much better using the parameters and thus the roles of these parameters are clearly determined. However, when the first lateral microplane starts softening, adjacent microplanes continue to resist higher and higher loads before they also start softening. Consequently, the whole fracture process on the macro scale overshoots the experimental data.

4.1.3 Iteration 3

In this iteration, the boundaries considered are as follows: The normal microplane boundaries for the lateral microplanes for tension and compression are given respectively by

$$\sigma^B_{Ntm} = C_1 E_t (h_1 \epsilon_N + S_1)\ e^{-(C_3 a_1)} \tag{4.16}$$

$$\sigma^B_{Ncm} = C_2 E_t (h_2 |\epsilon_N| + S_2)\ e^{-(C_4 a_2)} \tag{4.17}$$

in which $a_1 = <\epsilon_{Npt} - k_1>$, $a_2 = <\left|\epsilon_{Npc}\right| - k_2>$, ϵ_{Npt} is the maximum principal microplane strain, ϵ_{Npc} is the minimum principal microplane strain, C_1, C_2, C_3, C_4, h_1, h_2, S_1, S_2, k_1 and k_2 are adjustable parameters.

The normal microplane boundaries for the top microplane in tension and compression are given respectively by

$$\sigma^B_{Ntf} = E_l (h_3 \epsilon_N + S_3)\ \ e^{-(C_5 a_3)} \tag{4.18}$$

$$\sigma^B_{Ncf} = E_l (h_4 |\epsilon_N| + S_4)\ \ e^{-(C_6 a_4)} \tag{4.19}$$

in which $a_3 = <\epsilon_N - k_3>$, $a_4 = <|\epsilon_N| - k_4>$, C_5,C_6, h_3, h_4, S_3, S_4, k_3 and k_4 are adjustable parameters.

The L and M direction shear boundaries for lateral microplanes are given respectively by

$$\sigma^B_{Lf} = \frac{E_t}{1 + \nu_t}(h_5 |\epsilon_L| + S_5)\quad e^{-(C_7 a_5)} \tag{4.20}$$

$$\sigma^B_{Mm} = 2G_L (h_6 |\epsilon_M| + S_6)\quad e^{-(C_8 a_6)} \tag{4.21}$$

where $a_5 = <\left|\epsilon_{Lp}\right| - k_5>$, $a_6 = <\left|\epsilon_{Mp}\right| - k_6>$, C_7,C_8, h_5, h_6, S_5, S_6, k_5 and k_6 are adjustable parameters.

The L and M direction shear boundaries for the top microplane are given by the same boundary, defined as

$$\sigma^{B}_{L,Mf} = 2G_L(h_7 \left|\epsilon_{L,M}\right| + S_7)\ e^{-(C_9 a_{7,\mathrm{L,M}})} \tag{4.22}$$

in which $a_{7,L,M}$= <$\left|\epsilon_{L,M}\right|$ -k_7>, C_9, S_7, h_7 and k_7 are adjustable parameters.

Using the principal microplane stress in the boundaries of lateral microplanes allows the correct softening process for all lateral microplanes. In fact, in these formulations for lateral microplanes, when the first microplane with the maximum principal microplane stress trigger softening, the other side microplane, regardless of their microplane stress, start the softening process. This phenomenon can be explained by the experimental fact that when a part of the matrix (represented by the lateral microplanes) around the fiber begins to crack, the crack will grow in the matrix around the fiber rapidly.

However, it was found out that this boundary could achieve outstanding fits in all uniaxial loading paths but not in tansverse shear.

The normal microplane boundaries for the lateral microplanes for tension and compression have a determinant effect on the transverse shear. These boundaries cannot fit lateral and transverse shear loading paths simultaneously. Tuning the parameters for both lateral tension and compression loading path makes a sudden sharp drop before the fracture and unstable post-peak in transverse shear response.

In order to solve this problem, lateral microplane boundaries must respond differently to shear and lateral normal loadings. This problem is solved in the next iteration of formulations, and biaxial and multiaxial responses are improved.

4.1.4 The Final Iteration

In this final iteration, the normal microplane boundaries for the lateral microplanes for tension and compression are given respectively by

$$\sigma^B_{Ntm} = \frac{C_1}{E_t}(h_1\epsilon_N + S_1)\ \ e^{-(a_1+C_5a_2)} \tag{4.23}$$

$$\sigma^B_{Ncm} = \frac{C_2}{E_t}(h_2\,|\epsilon_N| + S_2)\ \ e^{-(a_1+C_6a_3)} \tag{4.24}$$

where $\epsilon_V = \epsilon_1 + \epsilon_2$ in the isotropy plane, $a_1 = C_3{<}\epsilon_V - k_1{>}$ if $\epsilon_V \geq 0$ and $a_1 = C_4{<}|\epsilon_V| - k_2{>}$ if $\epsilon_V < 0$, $a_2 = {<}\epsilon_{Npt} - k_3{>}$, $a_3 = {<}\left|\epsilon_{Npc}\right| - k_4{>}$, ϵ_{Npt} is the maximum principal microplane stress, ϵ_{Npc} is the minimum principal microplane stress, C_1, C_2, C_3, C_4, C_5, C_6 h_1, h_2, S_1, S_2, k_1, k_2, k_3 and k_4 are adjustable parameters.

The normal boundaries in tension and compression respectively for the top microplane are given by

$$\sigma^B_{Ntf} = E_l(h_3\epsilon_N + S_3)\ \ \ e^{-(C_7a_4)} \tag{4.25}$$

$$\sigma^B_{Ncf} = E_l(h_4\,|\epsilon_N| + S_4)\ \ \ e^{-(C_8a_5)} \tag{4.26}$$

where $a_4 = {<}\epsilon_N{+}(E_t/E_l)\,|\epsilon_V|\,{-}k_5{>}$, $a_5 = {<}\,|\epsilon_N|{+}(E_t/E_l)\,|\epsilon_V|\,{-}k_6{>}$, C_7,C_8, h_3, h_4, S_3, S_4, k_5 and k_6 are adjustable parameters.

The lateral microplane L and M-direction shear boundaries respectively are given by

$$\sigma^B_{Lm} = \frac{E_t}{1+\nu_t}(h_5\,|\epsilon_L| + S_5)\ \ \ e^{-(C_9a_6+a_1)} \tag{4.27}$$

$$\sigma^B_{Mm} = 2G_L(h_6\,|\epsilon_M| + S_6)\ \ \ e^{-(C_{10}a_7+a_1)} \tag{4.28}$$

where $a_6 = {<}\left|\epsilon_{Lp}\right| - k_7{>}$, $a_7 = {<}\left|\epsilon_{Mp}\right| - k_8{>}$, C_9,C_{10}, h_5, h_6, S_5, S_6, k_7 and k_8 are adjustable parameters.

The top microplane resultant shear boundary is given by

$$\sigma_{sf}^{B} = 2G_L(h_7\,|\epsilon_s| + S_7)\ \ e^{-(C_{11}a_8)} \tag{4.29}$$

in which $a_8 = <|\epsilon_s| - k_9>$, $\epsilon_s = \sqrt{{\epsilon_L}^2 + {\epsilon_M}^2}$, C_{11}, S_7, h_7 and k_9 are adjustable parameters.

In this boundary, ϵ_V solves the incompatibility problem between lateral and transverse shear loading path fitting. In fact, uniaxial lateral tension, lateral compression, and transverse shear loading path can fit experimental data with stable post-peak at the same time.

The main benefit of the using ϵ_V in boundary formulation of the lateral microplanes is that it allows fracture mechanism in lateral normal loading and shear loading to be differentiated. On the other hand, ϵ_V connects lateral loading to the top microplane. This improves the multiaxial loading response. The other advantage of this boundary formulation is that only eight lateral microplanes are sufficient to achieve good enough accuracy in the numerical calculations.

Although the meaning of adjustable and fixed parameters and the procedure for tuning them will be explained in detail later, we explain briefly how to obtain the values of these parameters as follows.

Except for C_1 and C_2, the C parameter values can be obtained from post-peak slope data fitting in uniaxial tension, compression, and shear loading in lateral and longitudinal directions. C_1 and C_2 can be tuned from the amplitude of lateral normal stress in uniaxial loading for tension and compression respectively.

The k parameters can be tuned by optimally matching the experimental peak stress location from uniaxial loading in lateral and longitudinal directions.

The S parameter values may be obtained by optimally approximating the nonlinearity initiation points in stress-strain test data of uniaxial loading in compression and tension for lateral and longitudinal directions.

Finally, the h parameters are obtained from optimally approximating the slope of nonlinear part of the stress-strain test data of uniaxial loading in compression and tension for lateral and longitudinal directions.

4.2 Cylindrical Microplane Model for Large Scale Simulations

In order to use the cylindrical microplane model for FRPs in large-scale simulations, the model is coded into the Abaqus/explicit VUMAT material subroutine. The subroutine is given in the Appendix.

Inside the main loop of the VUMAT for each Gauss point, first the previous state at the Gauss point is obtained from state variables. The state variables include previous values of the strain tensor components ϵ^0_{ij}, previous values of microplane stresses, σ^0_N, σ^0_M, σ^0_L and the state variable for deleting deformed elements.

To calculate the microplane strains and their increments, the initial value of strain tensor is available from the previous step, and in the VUMAT strain tensor increment is provided. The microplane stains are then calculated using Eqs3.2 and their increment is calculated as

$$\epsilon_{\mathrm{N}} = \mathrm{N_{ij}}\epsilon_{\mathrm{ij}} \quad \epsilon_{\mathrm{M}} = \mathrm{M_{ij}}\epsilon_{\mathrm{ij}} \quad \epsilon_{\mathrm{L}} = \mathrm{L_{ij}}\epsilon_{\mathrm{ij}} \tag{4.30}$$

$$\Delta\epsilon_{\mathrm{N}} = \mathrm{N_{ij}}\Delta\epsilon_{\mathrm{ij}} \quad \Delta\epsilon_{\mathrm{M}} = \mathrm{M_{ij}}\Delta\epsilon_{\mathrm{ij}} \quad \Delta\epsilon_{\mathrm{L}} = \mathrm{L_{ij}}\Delta\epsilon_{\mathrm{ij}} \tag{4.31}$$

Evaluation of the elastic stress tensor increment is evaluated using the strain tensor increment and elastic stiffness tensor, which is the inverse of the compliance tensor. In Voigt form, these equations read as

$$\Delta\sigma_I = S^{-1}_{IJ}\,\Delta\epsilon_{\mathrm{J}} \tag{4.32}$$

where I and J vary from 1 to 6.

The next steps in this section are the projection of the increment of elastic stress tensor onto the microplanes and calculating the current elastic microplane stresses and strains:

$$\Delta\sigma_{\mathrm{N}} = \mathrm{N}_{\mathrm{ij}}\Delta\sigma_{\mathrm{ij}} \quad \Delta\sigma_{\mathrm{M}} = \mathrm{M}_{\mathrm{ij}}\Delta\sigma_{\mathrm{ij}} \quad \Delta\sigma_{\mathrm{L}} = \mathrm{L}_{\mathrm{ij}}\Delta\sigma_{\mathrm{ij}} \tag{4.33}$$

$$\sigma_{\mathrm{N}} = \sigma_{N}^{0} + \Delta\sigma_{\mathrm{N}} \quad \sigma_{\mathrm{M}} = \sigma_{M}^{0} + \Delta\sigma_{\mathrm{M}} \quad \sigma_{\mathrm{L}} = \sigma_{L}^{0} + \Delta\sigma_{\mathrm{L}} \tag{4.34}$$

The loading and unloading on the microplanes are to be treated differently. If the loading path is unlcoading and $\epsilon_N \neq 0$, $\epsilon_M \neq 0$, $\epsilon_L \neq 0$ the microplane stresses are calculated as:

$$\sigma_{\mathrm{N}} = (\frac{\sigma_{N}^{0}}{\epsilon_{\mathrm{N}}})(\epsilon_{\mathrm{N}} + \Delta\epsilon_{\mathrm{N}}) \tag{4.35}$$

$$\sigma_{\mathrm{M}} = (\frac{\sigma_{M}^{0}}{\epsilon_{\mathrm{M}}})(\epsilon_{\mathrm{M}} + \Delta\epsilon_{\mathrm{M}}) \tag{4.36}$$

$$\sigma_{\mathrm{L}} = (\frac{\sigma_{L}^{0}}{\epsilon_{\mathrm{L}}})(\epsilon_{\mathrm{L}} + \Delta\epsilon_{\mathrm{L}}) \tag{4.37}$$

If the loading path is not unloading, in the next section of the algorithm the microplane boundaries σ^B_{Ntm}, σ^B_{Ncm} , σ^B_{Ntf} , σ^B_{Ncf}, σ^B_{Lm} , σ^B_{Mm} and σ^B_{sf} are calculated and imposed onto the microplane stresses. To this end, for the top microplane one has

$$\sigma_N = \max(\min\left(\sigma_N, \sigma^B_{Ntf}\right), -\sigma^B_{Ncf}) \tag{4.38}$$

$$\sigma_L = \min(\sigma_s , \sigma^B_{sf})\frac{\sigma_L}{\sigma_s} \tag{4.39}$$

$$\sigma_M = \min(\sigma_s , \sigma^B_{sf})\frac{\sigma_M}{\sigma_s} \tag{4.40}$$

where $\sigma_s = \sqrt{\sigma_L{}^2 + \sigma_M{}^2}$.

For the lateral microplanes one has:

$$\sigma_N = \max(\min\left(\sigma_N, \sigma^B_{Ntm}\right), -\sigma^B_{Ncm}) \tag{4.41}$$

$$\sigma_L = \min(|\sigma_L|, \sigma^B_{Lm})\frac{\sigma_L}{|\sigma_L|} \tag{4.42}$$

$$\sigma_M = \min(|\sigma_M|, \sigma^B_{Mm})\frac{\sigma_M}{|\sigma_M|} \tag{4.43}$$

Next, the excessively distorted elements should be deleted. Two indicators are used to determine if the element must be deleted: $|\epsilon_{pi}| > \epsilon_{max}$ and $|\epsilon_p| > \epsilon_{max}$. Here ϵ_{pi} and ϵ_p are the maxima of the absolute values of principal strains in the isotropy plane and the three-dimensional strain tensor. ϵ_{max} is the value of the maximum allowable strain for distortion. Once the conditions for deleting the element are satisfied, the state variable for element deletion is updated and thus the element is deleted. The last section of the algorithm calculates the final stress tensor using the stress equilibrium equation given by Eq 3.13. Finally, the state variables are updated.

4.3 Calibration of the Parameters

In order to calibrate the model for a specific FRP, uniaxial loading tests in the longitudinal direction, lateral direction, as well as in longitudinal shear and in transverse shear are needed. Although there are many parameters in the model, some parameters have little to no sensitivity to changes in the FRP type, so these parameters do not need to be calibrated. The meaning of all the parameters of the model which consitst of C-parameters, k-parameters, s-parameters and h-parameters are given in Table4.1, Table4.2, Table4.3 and Table4.4.

The parameter with default value	**The parameter determines**
$C_1 = 300$	the initial postpeak slope of the lateral direction stress-strain curve in tension
$C_2 = 100$	the initial postpeak slope of the lateral direction stress-strain curve in compression

$C_3 = 50$	the far postpeak slope of the lateral direction stress-strain curve in tension and transverse shear stress-strain curve
$C_4 = 50$	the far postpeak slope of the lateral direction stress-strain curve in compression and transverse shear stress-strain curve
$C_5 = 0.5$	the magnitude of lateral direction stress in tension
$C_6 = 0.5$	the magnitude of lateral direction stress in compression
$C_7 = 100$	the initial postpeak slope of longitudinal direction stress-strain curve in tension
$C_8 = 200$	the postpeak slope of longitudinal direction stress-strain curve in compression
$C_9 = 50$	the postpeak slope of transverse shear stress-strain curve
$C_{10} = 100$	the initial postpeak slop of along-the-fiber shear
$C_{11} = 100$	the far postpeak slope of along-the-fiber shear

Table 4.1: The C parameters used in the model, their default values and their roles

The parameter with default value	**The parameter determines the location of**
$k_1 = 0.001$	the peak stress on the lateral direction stress-strain curve in tension
$k_2 = 0.01$	the peak stress on the lateral direction stress-strain curve in compression

$k_3 = 0.03$	the onset point of softening on far postpeak in the lateral direction stress-strain curve in tension and the transverse shear stress-strain curve
$k_4 = 0.03$	the onset point of softening on far postpeak in the lateral direction stress-strain curve in compression and the transverse shear stress-strain curve
$k_5 = 0.02$	the peak stress on the longitudinal direction stress-strain curve in tension
$k_6 = 0.02$	the peak stress on the longitudinal directionstress-strain curve in compression
$k_7 = 0.01$	the peak stress on the transverse shear stress-strain curve
$k_8 = 0.03$, $k_9 = 0.02$	the peak stress on the along-the-longitudinal direction shear stress-strain curve

Table 4.2: The k parameters used in the model, their default values and their roles

The parameter with default value	**The parameter determines the location of**
$s_1 = 0.01$	the onset point of inelasticity in the lateral direction stress-strain curve in tension
$s_2 = 0.015$	the onset point of inelasticity in the lateral direction stress-strain curve in compression
$s_3 = 0.01$	the onset point of inelasticity of longitudinal direction stress-strain curve in tension
$s_4 = 0.005$	the onset point of inelasticity in longitudinal direction stress-strain curve in compression

$s_5 = 0.002$	the onset point of inelasticity in transverse shear stress-strain curve
$s_6 = 0.0025$	the onset point of initial inelasticity in along-the-fiber shear stress-strain curve
$s_7 = 0.0025$	the onset point of near peak inelasticity in along-the-fiber shear stress-strain curve

Table 4.3: The s parameters used in the model, their default values and their role

The parameter with default value	**The parameter determines**
$h_1 = 1.5$	the prepeak slope of nonlinearity in the lateral direction stress-strain curve in tension
$h_2 = 1.5$	the prepeak slope of nonlinearity in the lateral direction stress-strain curve in compression
$h_3 = 0.5$	the prepeak slope of nonlinearity in fiber direction stress-strain curve in tension
$h_4 = 0.5$	the prepeak slope of nonlinearity in fiber direction stress-strain curve in compression
$h_5 = 1$	the prepeak slope of nonlinearity in transverse shear stress-strain curve
$h_6 = 0.5$, $h_7 = 0.5$	the slopes of initial nonlinearity and near-peak nonlinearity respectively in longitudinal shear stress-strain curve.

Table 4.4: The h parameters used in the model, their default values and their roles

4.4 Calibration Procedure

It may seem that there are many parameters in the model, but these parameters can be calibrated easily for any transversely isotropic FRP. The calibration procedure includes four steps; however, in some problems it may not be necessary to tune all parameters, and thus they can be kept at their default values. The calibration should start with the parameters set to their default values given in Table4.1, Table4.2, Table4.3 and Table4.4. The calibration procedure consists of the determineation of first the k-parameters, next the s-parameters, followed by the h-parameters and finally the C-parameters. To this end, the following steps must be carried out:

1. k_1 must be determined by optimally fitting uniaxial tension test data in the lateral direction.
2. k_2 must be determined by optimally fitting uniaxial compression test data in the lateral direction.
3. k_3, k_4 and k_7 must be determined by optimally fitting transverse shear stress versus transverse shear strain data.
4. k_5 must be determined by fitting uniaxial tension test data in the longitudinal direction.
5. k_6 must be determined by fitting uniaxial compression test data in the longitudinal direction.
6. k_8 and k_9 must be determined by optimally fitting longitudinal shear stress versus longitudinal shear strain data.
7. s_1 must be determined by optimally fitting uniaxial tension test data in the lateral direction.
8. s_2 must be determined by optimally fitting uniaxial compression test data in the lateral direction.

9. s_3 must be determined by optimally fitting uniaxial tension test data in the longitudinal direction.
10. s_4 must be determined by optimally fitting uniaxial compression test data in the longitudinal direction.
11. s_5 must be determined by optimally fitting transverse shear stress versus transverse shear strain data.
12. s_6 and s_7 must be determined by optimally fitting longitudinal shear stress versus longitudinal shear strain data.
13. h_1 must be determined by optimally fitting uniaxial tension test data in the lateral direction.
14. h_2 must be determined by optimally fitting uniaxial compression test data in the lateral direction.
15. h_3 must be determined by optimally fitting uniaxial tension test data in the longitudinal direction.
16. h_4 must be determined by optimally fitting uniaxial compression test data in the longitudinal direction.
17. h_5 must be determined by optimally fitting transverse shear stress versus transverse shear strain data.
18. h_6 and h_7 must be determined by optimally fitting longitudinal shear stress versus longitudinal shear strain data.
19. C_1 and C_3 must be determined from optimally fitting uniaxial tension test data in the lateral direction.
20. C_2 and C_4 must be determined from optimally fitting uniaxial tension test data in the lateral direction.

21. C_7 must be obtained from optimally fitting uniaxial tension test data in the longitudinal direction.

22. C_8 must be determined by optimally fitting uniaxial compression test data in the longitudinal direction.

23. C_9 must be determined by optimally fitting transverse shear stress versus transverse shear strain data.

24. C_{10} and C_{11} must be determined by optimally fitting along-the-fiber shear stress vs along-the-fiber shear strain data.

25. C_5 and C_6 must be kept at their default values generally. However, they can be obtained from lateral direction pre-peak data fitting if necessary.

The C parameters are known to have little to no sensitivity to changes in the FRP type, whereas the k parameters should be calibrated for different FRPs. The s and h parameters (onset points of behavior change and slopes at these points, respectively) are to be calibrated for different FRPs as well.

Chapter 5

Verification

The complete mechanical characterization of a transversely isotropic FRP consists of a total of 6 different test data on lateral direction compression and tension, longitudinal direction compression and tension, longitudinal shear and transverse shear. Unfortunately, such experimental data in the literature for the same FRP is limited. However, relatively extensive test data are found for AS4/3501-6 carbon/epoxy and E-glass/MY750 epoxy in the publications by Soden et al [65, 66]. Moreover, the size effect test data from three-point bending tests reported in [67] on carbon fiber/epoxy are useful to verify the model. To verify the model further, open-hole fracture experimental data on FRP called IM7/8552 obtained form [68] are to be simulated as well.

In crack band models, element size is considered as the characteristic length. The model developed in this work is meant to be in the sense of the crack band model. That means, the model parameters are optimized for a cubic hexahedral element with a side length of 0.5mm unless a different size is indicated in this section. Other element sizes may certainly be used, but the model needs to be recalibrated for the selected new size elements following the same calibration procedured discussed in the previous section.

One issue in crack band models is that cracks tend to follow the mesh lines, which creates a certain mesh bias in the results. In this study, meshes are chosen to minimize such interference of arbitrary meshes. The case of arbitrary meshes used in the sense of crack band model to predict material response is a chanllenging problem which is not within the scope of this study.

5.1 The Carbon/Epoxy FRP Composite “AS4/3501-6”

The carbon/epoxy FRP composite AS4/3501-6 is used in many engineering applications such as chassis, brakes, interior structural elements, exterior structural elements, and the body in automotive, aerospace, aviation, marine, rail, and mass transit industries. In Table5.1, the properties of AS4/3501-6 are given.

Fiber type	AS4
Matrix type	3501-6 Epoxy
Transverse modulus, E_t	11 GPa
Longitudinal modulus, E_l	126 GPa (initial modulus)
Longitudinal shear modulus,G_l	6.6 GPa
Major Poisson’s ratio, ν_t	0.4
Through-thickness Poisson’s ratio, ν_l	0.28
Fiber volume fraction, ν_f	60%
Longitudinal tensile strength	1950 MPa
Longitudinal compressive strength	1480 MPa
Transverse tensile strength	48 MPa
Transverse compressive strength	200 MPa

Table 5.1: Properties of the carbon/epoxy FRP composite AS4/3501-6.

The optimum parameter values determined using the procedure discussed in Section 3.4 are given in Table5.2.

Parameter	**Value**	**Parameter**	**Value**
C_1	400	k_7	0.01
C_2	100	k_8	0.02
C_3	50	k_9	0.015
C_4	50	s_1	0.01
C_5	0.454	s_2	0.011
C_6	0.454	s_3	0.0067
C_7	100	s_4	0.0045
C_8	200	s_5	0.0025
C_9	50	s_6	0.0025
C_{10}	100	s_7	0.0025
C_{11}	120	h_1	1.5
k_1	0.0013	h_2	1.4
k_2	0.0128	h_3	0.5
k_3	0.03	h_4	0.5
k_4	0.03	h_5	1
k_5	0.018	h_6	0.5
k_6	0.015	h_7	0.8

Table 5.2: Optimum parameter values for carbon/epoxy FRP composite AS4/3501-6

For the longitudinal direction tension, the comparison of the simulation results using the present model and experimental data are shown in Fig5.1. In this simulation,a prismatic specimen with a rectangular cross section is considered. The specimen is 16.5mm in length, 10mm in height, and 5mm in width. Hexahedral elements of 0.5mm in size are used in the mesh, and the longitudinal direction is taken to be parallel to the loading. A velocity of 0.01 mm/s is applied as tensile loading. The specimen had a notch in the form of an isosceles triangular prism with a height of 0.5mm and base dimensions of 0.25mm by 5mm at the mid section. A single transverse crack is observed to start from the notch tip in longitudinal tension and to propagate across the cross-section perpendicular to the loading.

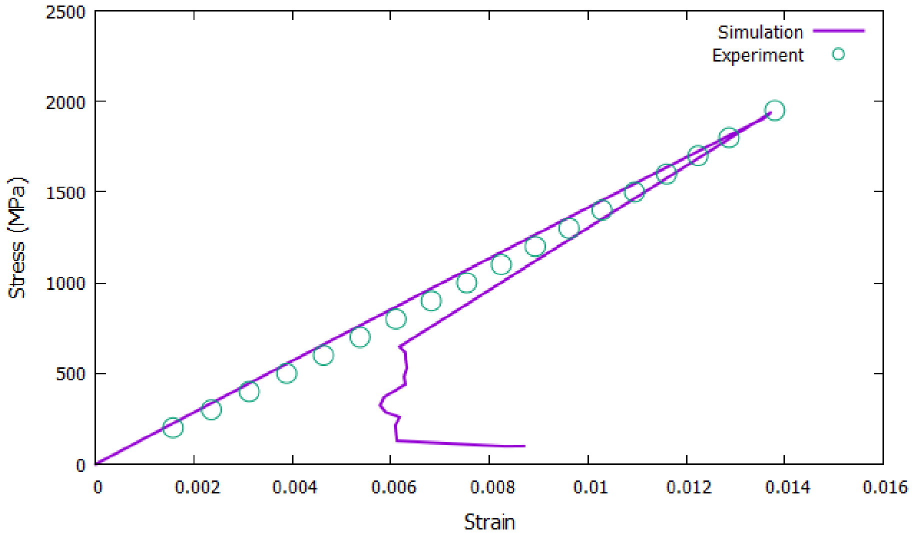

Figure 5.1: Simulation of the longitudinal tension test for AS4/3501-6 and comparison to test data

The Fig5.2 compares the test data and the simulation of the same test in longitudinal compression. The same specimen from the longitudinal tension simulation is used for longitudinal compression as well. Hexahedral elements with the same size of 0.5mm are used to create the mesh. The crack path for the entire load-displacement curve in longitudinal direction compression is shown in Fig5.3, which is similar to the experimentally observed damage patterns given in [69].

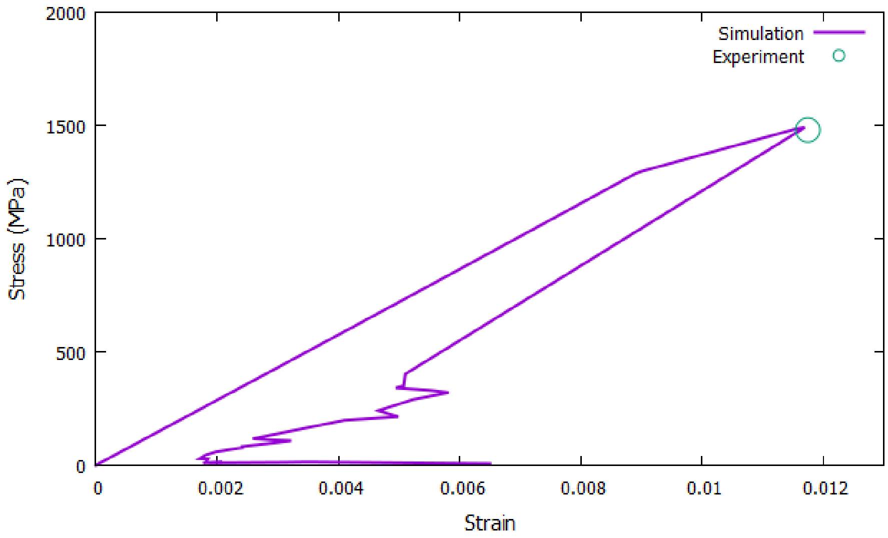

Figure 5.2: Simulation of the longitudinal compression test for AS4/3501-6 and comparison to test data

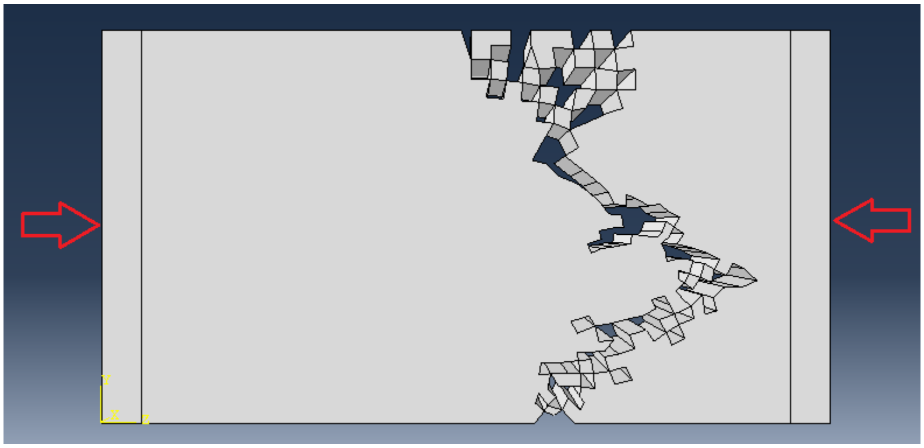

Figure 5.3: The crack path obtained in the simulation of longitudinal compression for AS4/3501-6

The compression simulation and test data in compression for this FRP in the lateral direction are compared in Fig5.4. The specimen has the same dimensions as in longitudinal tension and compression simulations, but the fiber direction is taken as perpendicular to the fibers. Compressive loading is applied at a velocity of 0.01mm/s. The specimen has a notch with the same dimensions as in longitudinal direction tension simulation at the mid section. The crack path for the entire load history is given in Fig5.5. Typically in the unidirectional FRPs subjected to transverse compression, the crack propagates at an angle of approximately 50° to 56° relative to the longitudinal direction. In the simulation, the obtained crack path has an average inclination of 45°.

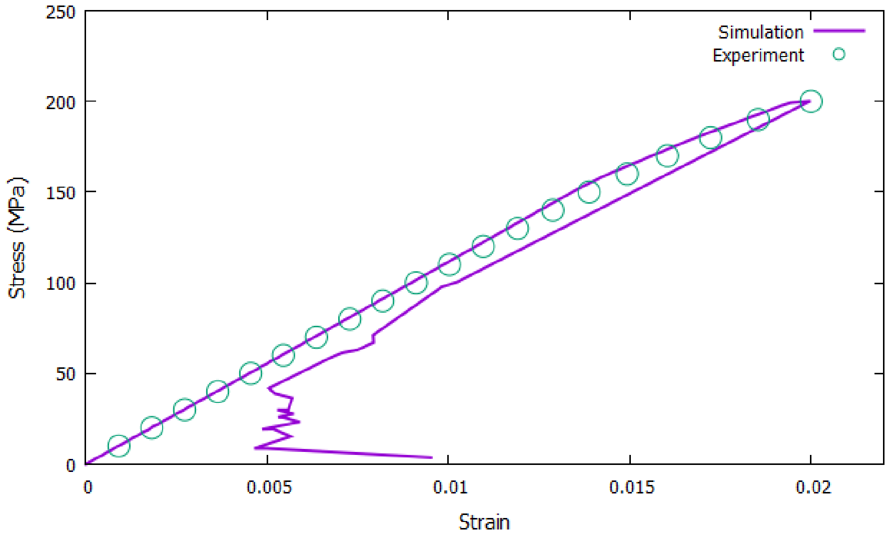

Figure 5.4: The simulation of lateral direction compression for AS4/3501-6 and comparison to test data

Figure 5.5: The simulated crack path in lateral compression for AS4/3501-6

The lateral direction tension simulation and test data are compared in Fig5.6. The same notched specimen as in longitudinal compression, longitudinal tension and lateral compression simulations is used in this simulation. The element type is hexahedral and the element size is strictly the same size, 0.5mm. In the lateral direction tension simulation, the crack starts from the notch tip and develops perpendicular to fibers until it crosses the entire cross section.

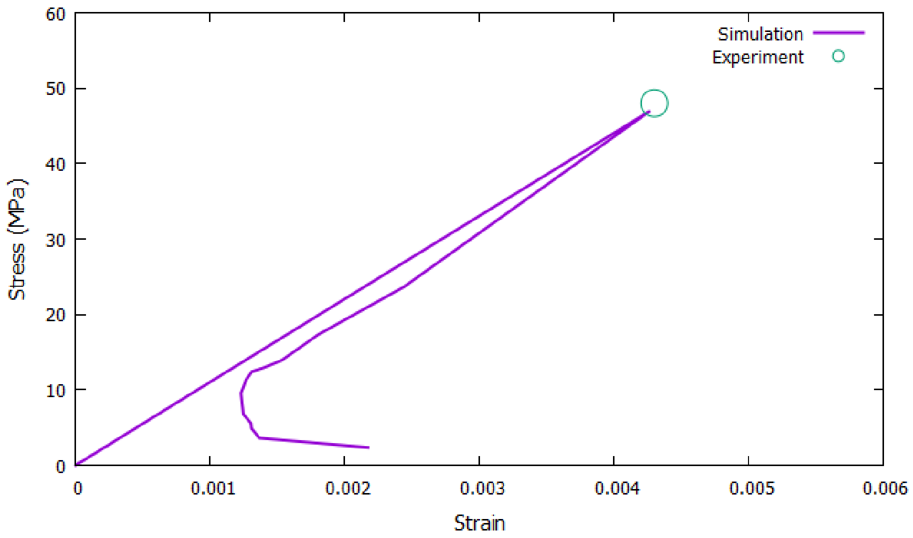

Figure 5.6: The simulation of lateral direction tension and comparison to test data for AS4/3501-6

The Fig5.7 compares the simulated longitudinal shear behavior and test data. The specimen for this simulation is a thin-walled cylinder loaded in torsion. The outer and inner radii of the cylinder are 3mm and 3.5mm respectively and the length of the cylinder is 20mm. Hexahedral elements are used to create the mesh and the same element size of 0.5mm is employed. The experimental data do not include the post-peak softening. The reason may be snap-back behavior of the specimen that results from the stiffness of the testing machine being too low or the size of the specimen being too large or both [60].

The post-peak snap-back response of the specimens could easily be captured using the so called arc-length method available for implicit finite element solvers [70]. For explicit finite element solvers, however, there is no option to automatically capture the snap-back response. In this study, the post-peak snap-back curves in Figs 5.1,5.2, 5.6 and 5.4 are simulated as follows:

1. Delete the distorted elements, if there are any, using the criteria of maximum principal isotropy plane strain $\epsilon_{max} \geq 3\%$,
2. unload to zero just before the loss of stability in the calculations,
3. reload to produce further fracture and go to the first step above; continue this loop until the post-peak snap-back curve is obtained completely.

In the crack band models the fracture energy, and thus the area below the load-displacement curve, depend on element size [45]. In other words, in this class of models the element width perpendicular to the crack is the localization limiter. Because the crack can grow in any direction, the element size becomes the localization limiter. If the element size is altered, the model should be recalibrated to obtain the same fracture energy using the new element size. Thus, with the new element size, the values of the adjustable parameters would be different but the simulated response would essentially be the same.

The alternative to keeping the element size as the localization limiter is a nonlocal version of this model in which the localization limiter is specified externally and the element size becomes arbitrary. Such a model would obviously be tremendously useful. It will be tackled in a future study. In this study the use of Abaqus/Explicit user subroutine feature limits the possibility of developing a nonlocal version of this model.

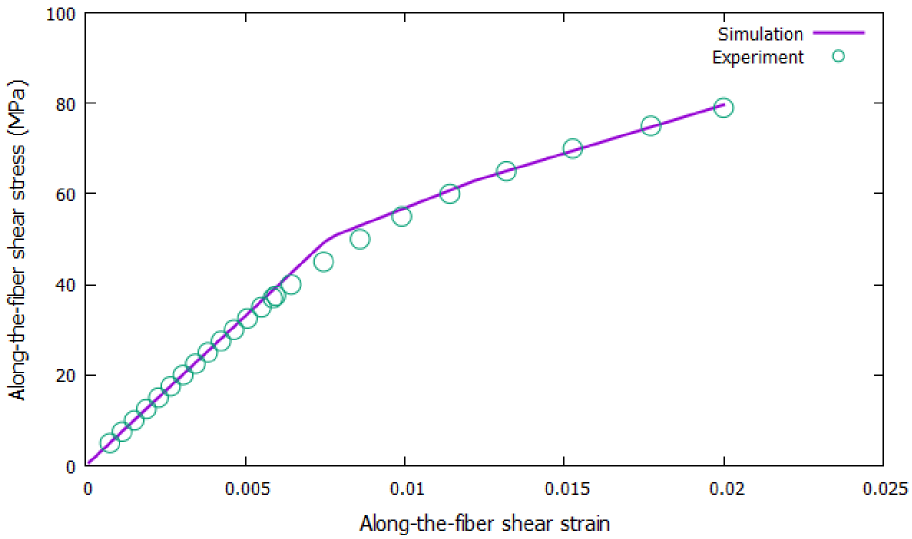

Figure 5.7: The simulated stress-strain curve in along-the-fiber shear for AS4/3501-6

The calibrated model is now used to *predict* the biaxial failure envelope from [50] as shown in Fig5.8. The prismatic notchless specimen in this simulation has the dimensions of $5 \times 5 \times 2$mm. The element type is hexahedral, and the element size is taken strictly as 0.5mm. In Fig5.8, the load path is first loading in the lateral direction followed by loading in the longitudinal direction until failure is reached. The figure shows that the model prediction and the test data agree well.

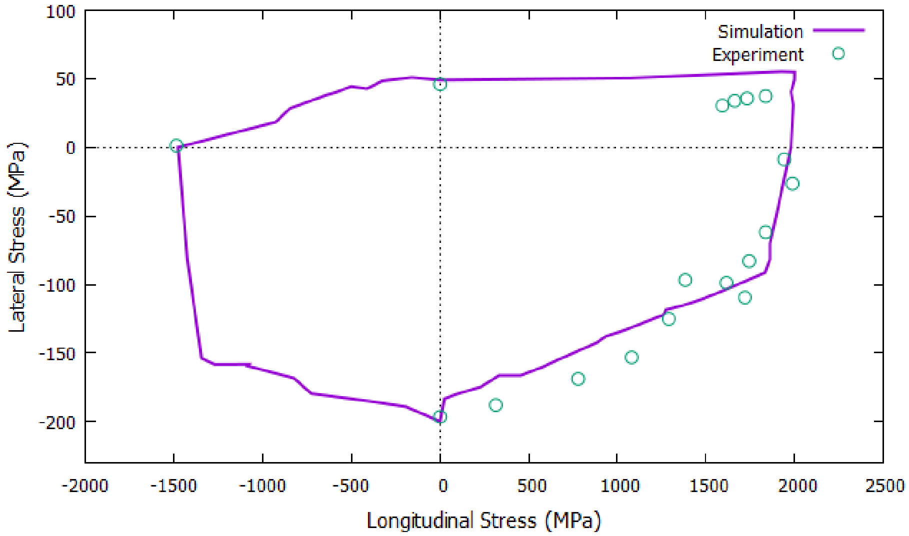

Figure 5.8: The predicted biaxial failure envelope and comparison to experimental data for AS4/3501-6

5.2 The Glass/Epoxy FRP Composite “E-glass/MY750 epoxy”

Another FRP for which a relatively wide range of experimental data is available in the literature is E-glass/MY750 epoxy, widely used for many engineering applications. The properties of this FRP are shown in Table 5.3.

Fiber type	Silenka E-Glass 1200tex
Matrix type	MY750/HY917/ DY063 Epoxy
Transverse modulus, E_t	16.2 GPa
Longitudinal modulus, E_t	45.6 GPa
Longitudinal shear modulus,G_l	5.83 GPa

Major Poisson's ratio, ν_t	0.4
Through-thickness Poisson's ratio, ν_l	0.278
Fiber volume fraction, ν_f	62%
Longitudinal tensile strength	1280 MPa
Longitudinal compressive strength	800 MPa
Transverse tensile strength	40 MPa
Transverse compressive strength	145 MPa

Table 5.3: The properties of E-glass/MY750 epoxy

Table5.4 illustrates the optimum parameter values obtained from the calibration procedure applied to the test data for E-glass/MY750 epoxy.

Parameter	**Value**	**Parameter**	**Value**
C_1	600	k_7	0.01
C_2	130	k_8	0.04
C_3	50	k_9	0.01
C_4	50	s_1	0.01
C_5	0.308	s_2	0.0115
C_6	0.308	s_3	0.014
C_7	100	s_4	0.0092
C_8	200	s_5	0.002
C_9	50	s_6	0.0014
C_{10}	100	s_7	0.0035

C_{11}	90	h_1	1.5
k_1	0.00055	h_2	1.1
k_2	0.0085	h_3	0.52
k_3	0.03	h_4	0.5
k_4	0.03	h_5	1
k_5	0.035	h_6	0.25
k_6	0.0226	h_7	0.9

Table 5.4: The optimum parameter values for E-glass/MY750 epoxy

For the longitudinal direction tension, simulation results using the model and the comparison to experimental data are shown in Fig 5.9. In this simulation, the same notched specimen used in the previous simulations is used. Hexahedral elements with a size of 0.5mm are employed to create the mesh. Tensile loading in this simulation is prescribed as a velocity of 0.01mm/s. During the simulation, a single transverse crack starts from the notch tip and propagates across the fibers perpendicular to the loading.

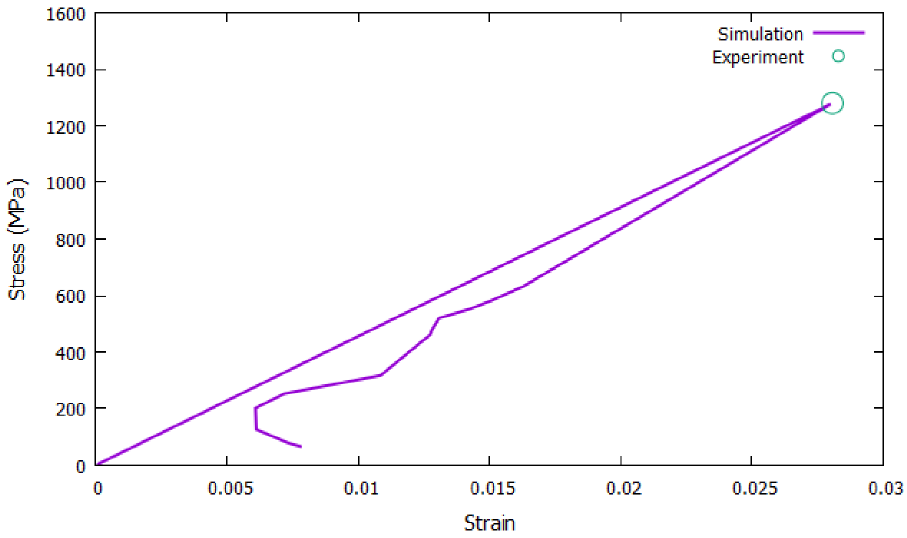

Figure 5.9: The simulated stress-strain response in longitudinal tension for E-glass/MY750 Epoxy and comparison to experimental data

In Fig5.10 the longitudinal compression behavior as simulated is compared to the test data. The notched specimen is the same as in the previous simulations and the element size and type are also the same. The compressive loading is applied at a velocity of 0.01mm/s. Fig5.11 shows the corresponding crack path.

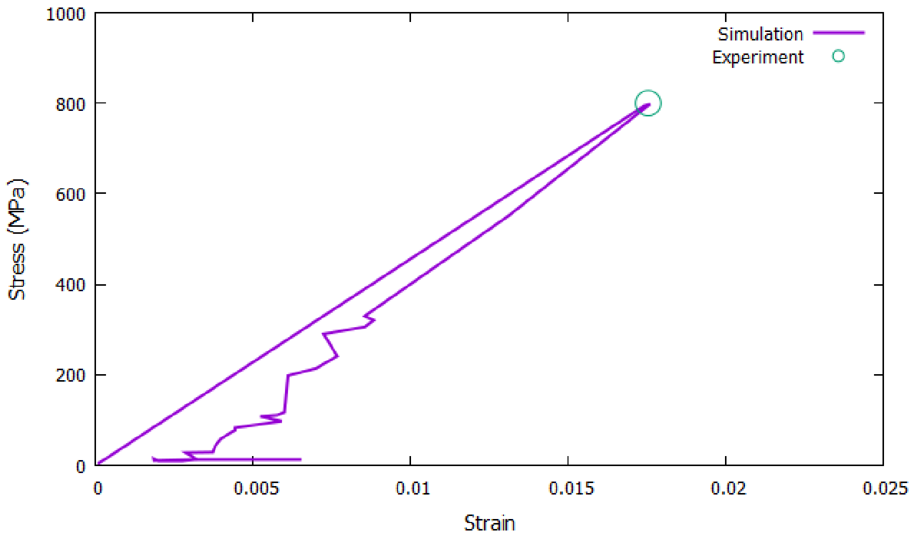

Figure 5.10: Simulated stress-strain response in longitudinal compression for E-glass/MY750 Epoxy and comparison to experimental data

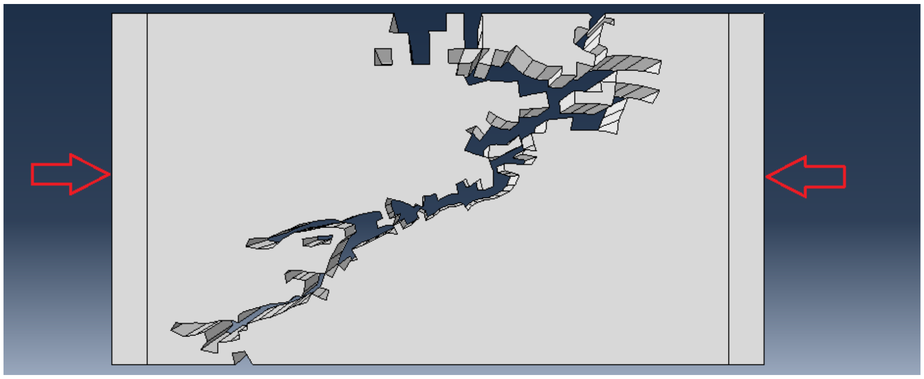

Figure 5.11: The crack path for longitudinal compression for E-glass/MY750 epoxy

The compression and tension behaviors in the lateral direction are compared to experimental data in Figs5.12 and 5.13. The notched specimen is the same specimen in the previous simulations and the element size is the same as well. Furthermore, both compressive and tensile loadings are applied at a velocity of 0.01 mm/s. In Fig5.14 , the crack path in compression is shown. It is observed that during the simulations in tension, a single transverse crack starts from the notch tip in the lateral direction and propagates across the cross-section perpendicular to the loading.

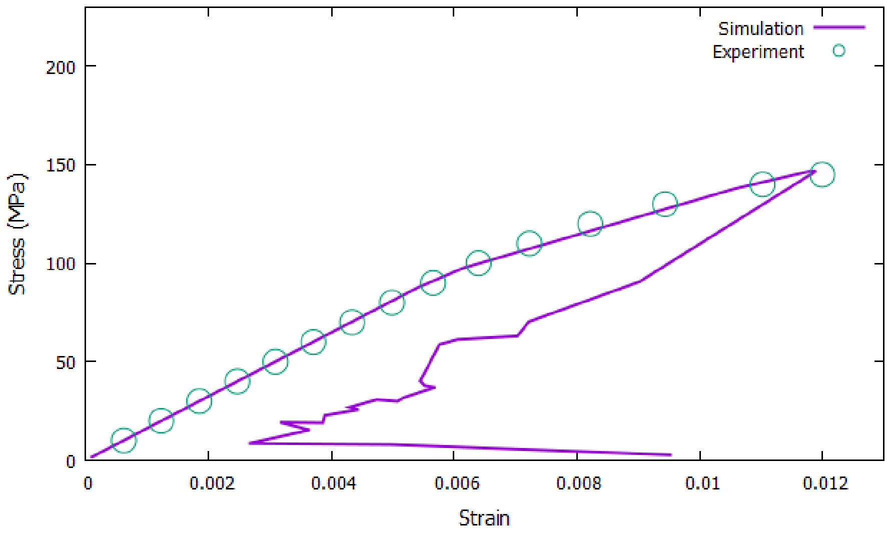

Figure 5.12: Simulated stress-strain response in lateral compression for E-glass/MY750 Epoxy and comparison to experimental data

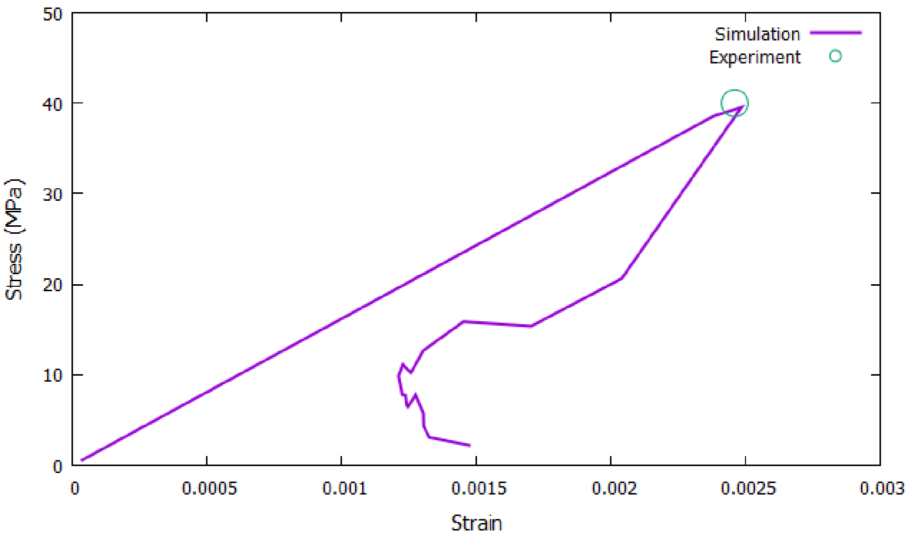

Figure 5.13: Simulated stress-strain response in lateral tension for E-glass/MY750 Epoxy and comparison to experimental data

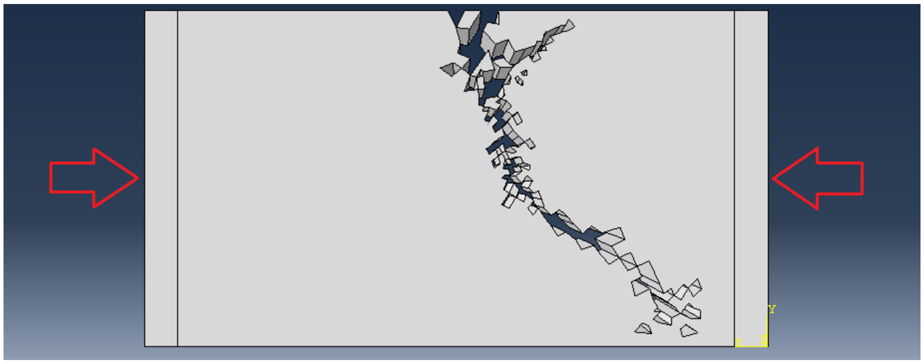

Figure 5.14: The crack path in lateral compression for E-glass/MY750 Epoxy

The along-the fiber shear calibration of the model yields the shear behavior as shown in Fig5.15, which compares very favorably against the experimental data. The specimen for this simulation is the same thin-walled cylinder under torsion used for AS4/3501-6. Again hexahedral elements with an element size of 0.5mm are used for the mesh.

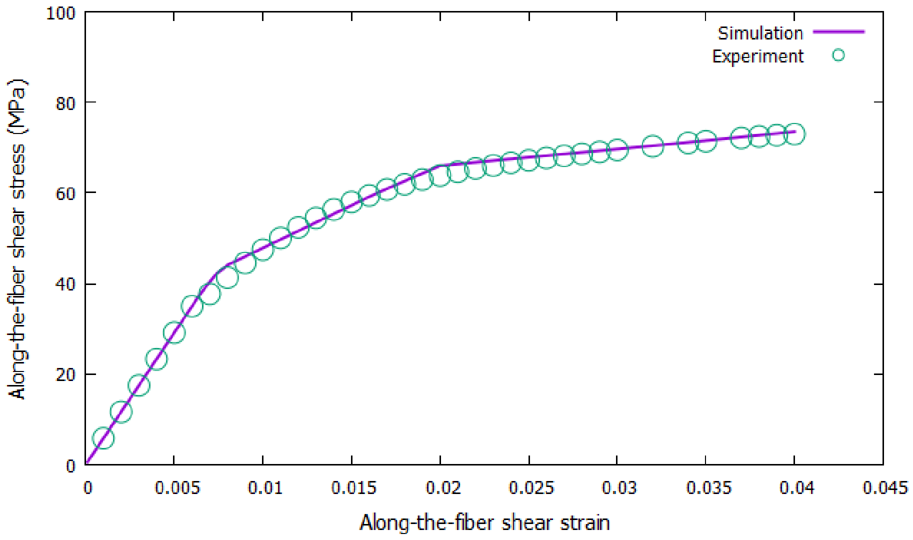

Figure 5.15: Simulated stress-strain response in along-the-fiber direction shear loading for E-glass/MY750 Epoxy and comparison to experimental data

The calibrated model is now used to predict its biaxial failure envelope, as shown in Fig5.16. The simulated curve is obtained by first loading in the lateral direction and then loading in the longitudinal direction until failure is reached. The simulated response clearly matches the experimental data very closely. In this case, the fibers are oriented at 85°, and because of the relatively weak matrix in the lateral direction, along with the cracking perpendicular to fibers there is also cracking in the matrix along the fibers. The simulated crack path is approximately at 55° relative to the longitudinal direction.

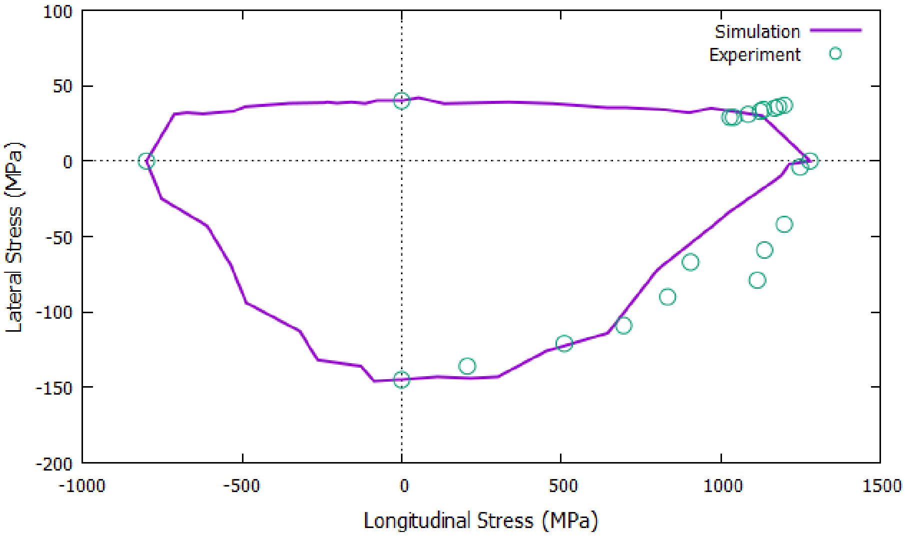

Figure 5.16: The Biaxial Failure Envelope for E-glass/MY750 Epoxy

5.3 The FRP Composite "Carbon fiber/epoxy"

Waas and coauthors [67] have carried out the so-called "size effect" [45] tests on geometrically similar specimens in 3pt-bending. The laminates are made up of carbon fiber/epoxy laminae with a stacking sequence of [-45/0/45/90]. The test configuration is illustrated in Fig5.17. The dimensions in Fig5.17 are for size 1X, and four other specimens have proportional sizes scaled as 1.5X, 2X, 3X, and 4X, which mean that all dimensions of a specimen are obtained by multiplying the corresponding dimensions of the smallest specimen by 1.5, 2, 3 or 4.

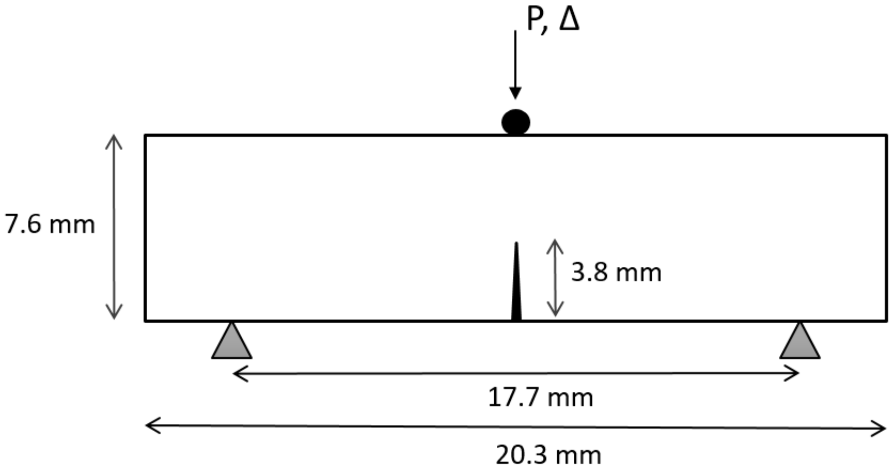

Figure 5.17: The test configuration of 3-Point bending for Carbon Fiber/Epoxy

The thickness of all specimens is 6.35mm. Unlike most test data on FRPs, these test data have a stable post-peak. The element size used in the simulations is 0.633mm and the critical max principal strain for element deletion is taken as ϵ_{max} = 2.5%. In Table5.5 the properties of the carbon fiber/epoxy laminas are shown.

Fiber type	Carbon
Matrix type	Epoxy
Transverse modulus, E_t	6.7 GPa
Longitudinal modulus, E_t	141 GPa
Longitudinal shear modulus,G_l	3.2 GPa
Major Poisson's ratio, ν_t	0.4
Through-thickness Poisson's ratio, ν_l	0.33
Fiber volume fraction, ν_f	55%
Longitudinal tensile strength	1900 MPa
Longitudinal compressive strength	1300 MPa

Transverse tensile strength	50 MPa
Transverse compressive strength	230 MPa

Table 5.5: The properties of Carbon Fiber/Epoxy

Unfortunately the 6 different test data for individual carbon fiber/epoxy lamina needed to uniquely calibrate the model are not available in this case. Consequently, the aforementioned calibration procedure cannot be applied. Instead, starting with the default values of all parameters, the free parameters are adjusted in order to fit the largest size specimen force-displacement test data, as shown in Fig5.18. In this figure, the force and displacement values are normalized with respect to the maximum respective values for the largest size, which are 3970N and 1.43mm. In Table5.6, the optimum parameter values obtained by optimally fitting the largest specimen force-displacement data are shown.

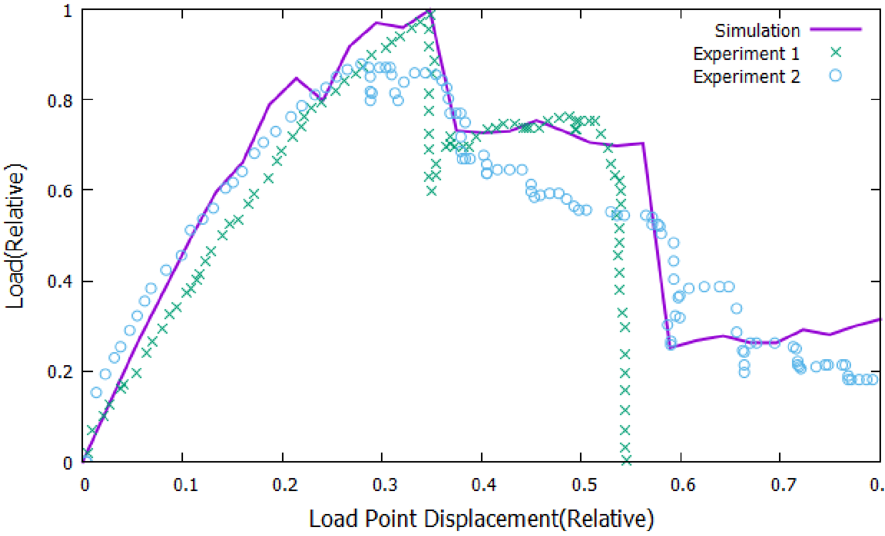

Figure 5.18: Simulated load displacement curve compared to experimental data for size D=30.4mm

Parameter	**Value**	**Parameter**	**Value**
C_1	200	k_7	0.01
C_2	100	k_8	0.02
C_3	50	k_9	0.015
C_4	50	s_1	0.01
C_5	0.746	s_2	0.015
C_6	0.746	s_3	0.0067
C_7	100	s_4	0.0045
C_8	200	s_5	0.002
C_9	50	s_6	0.0025
C_{10}	100	s_7	0.0025
C_{11}	120	h_1	1.5
k_1	0.0013	h_2	1.4
k_2	0.0228	h_3	0.5
k_3	0.03	h_4	0.5
k_4	0.044	h_5	1
k_5	0.02	h_6	0.5
k_6	0.012	h_7	0.8

Table 5.6: The optimum parameter values for Carbon Fiber/Epoxy composite

The calibrated model is used in the *prediction* of force-displacement behavior of other size specimens without changing any parameter values. In Fig5.19 the model prediction and experimental data for size 1X are compared. Clearly the model prediction closely approximates the experimental data.

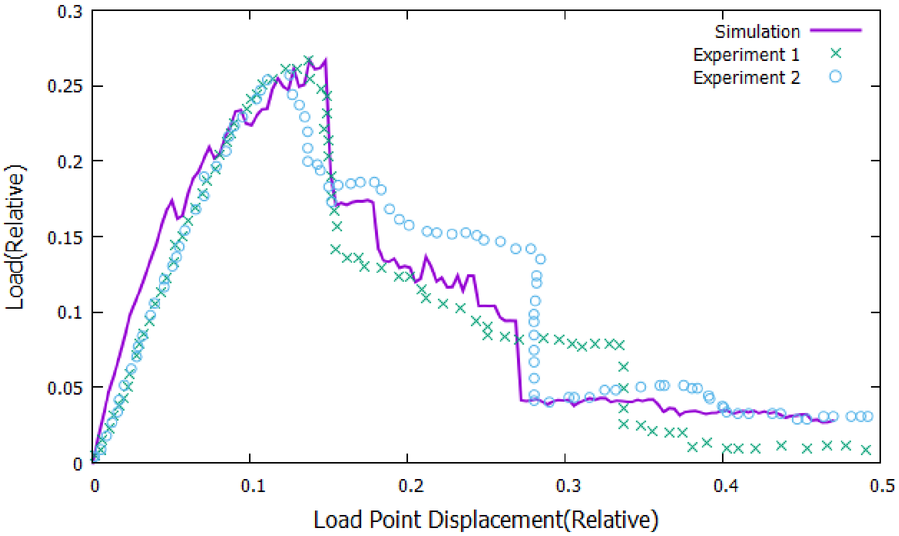

Figure 5.19: The predicted load displacement curve compared to experimental data for size D=7.6mm

The model prediction for force-displacement behavior of the specimen with size 1.5X and the associated experimental data are compared in Fig5.20. The figure shows that the model prediction closely approximates the test data, although the peak load could not be approximated very closely.

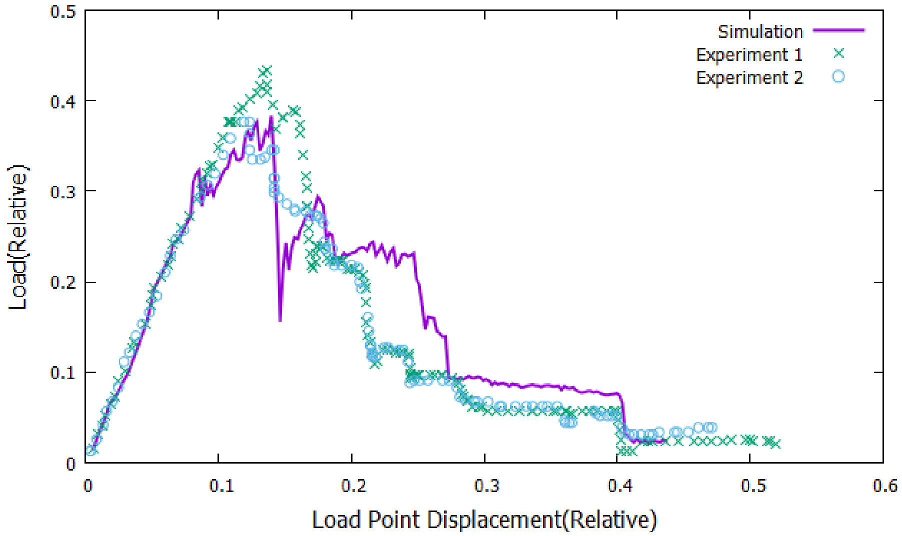

Figure 5.20: The predicted load displacement curve compared to experimental data for size D=11.4 mm

The predicted force-displacement behavior for size 2X and comparison to experimental data are shown in Fig5.21. The figure shows that the model prediction and experimental data agree very well.

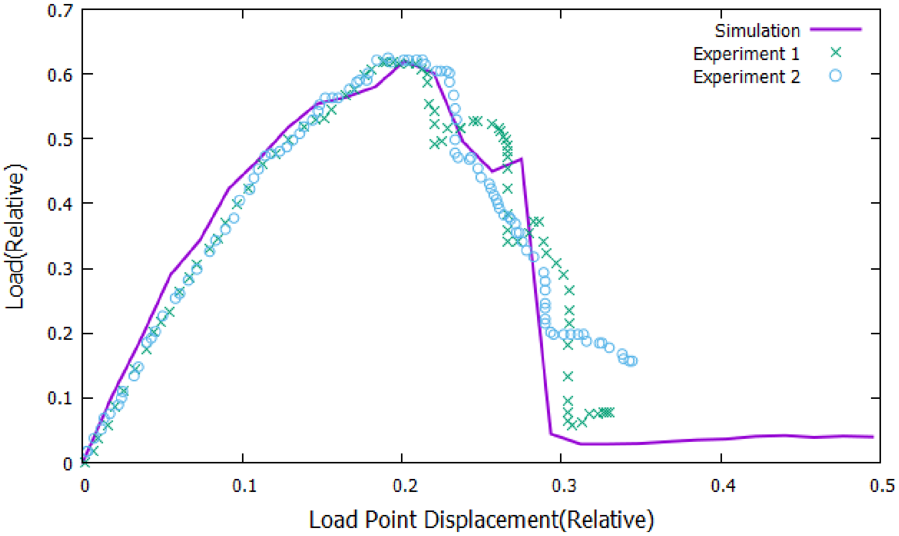

Figure 5.21: The predicted load displacement curve compared to experimental data for size D=15.2 mm

Fig5.22 compares force-displacement behavior prediction with the associated experimental data for size 3X. The model prediction is very close to the experimental data for one of the specimens. The differences between the experimental data from two different specimens are attributable to statistical effects on the specimen cross sectional microstructure.

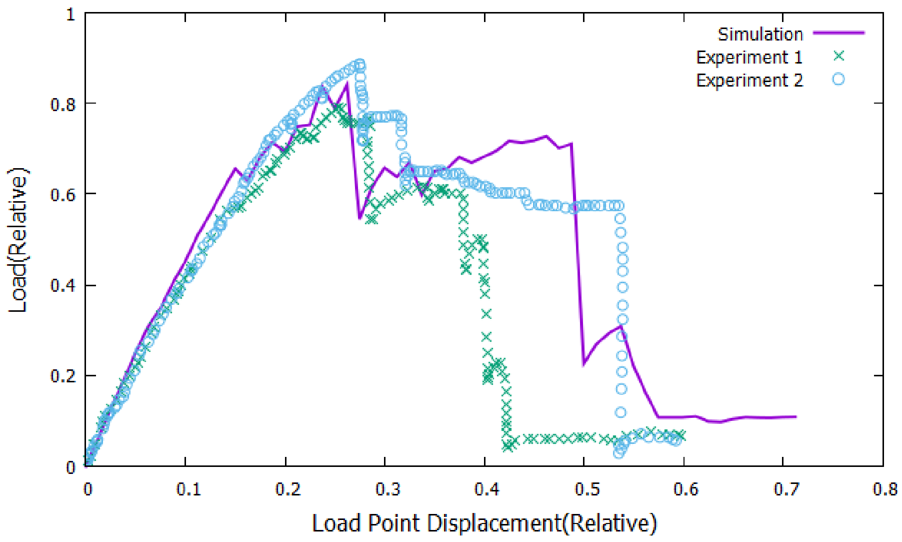

Figure 5.22: The predicted load displacement curve compared to experimental data for size D=22.8 mm

In Figs5.18, 5.19, 5.20, 5.21 and 5.22, the model predictions approximate the experimental data very closely. The averaged absolute value of errors normalized with respect to the maximum force measured in the tests for sizes 1X, 1.5X, 2X, 3X, and 4X are as low as 0.051, 0.073, 0.031, 0.092, 0.045, respectively. Generally the crack starts from the notch tip and propagates across the cross-section to the loading point in all specimens, although the crack path is ususally jagged. Fig 5.23 shows the typical predicted crack path for the size 1.5X.

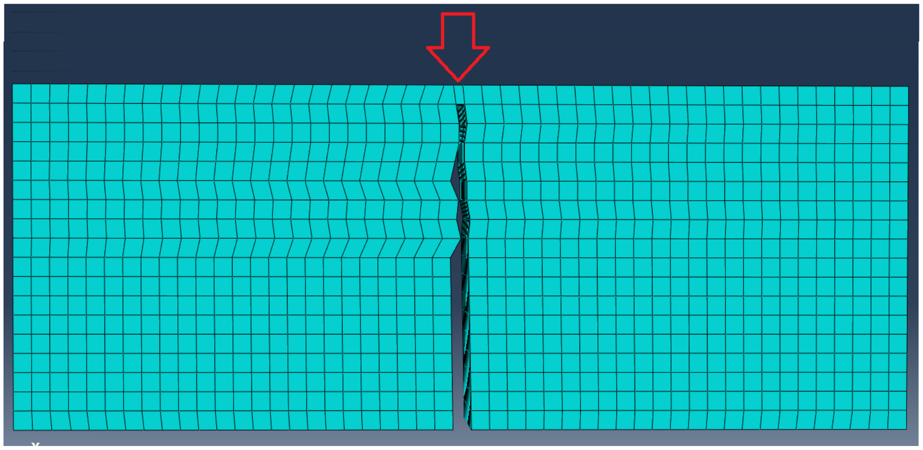

Figure 5.23: The predicted crack path for size D=11.4 mm

5.4 The Carbon/Epoxy FRP Composite "IM7/8552 Carbon-Fiber/Epoxy"

To further verify the model, it has been used to simulate the open-hole specimen strength data for the FRP called "IM7/8552 carbon-fiber/epoxy". In Table5.7 the relevant properties of this FRP are shown.

Fiber type	IM7
Matrix type	8552
Transverse modulus, E_t	11.38 GPa
Longitudinal modulus, E_t	161 GPa
Longitudinal shear modulus,G_l	5.17 GPa
Major Poisson's ratio, v_t	0.436
Through-thickness Poisson's ratio, v_t	0.32
Fiber volume fraction, v_f	65%

Longitudinal tensile strength	2723 MPa
Longitudinal compressive strength	1300 MPa
Transverse tensile strength	60 MPa
Transverse compressive strength	276 MPa

Table 5.7: The properties of IM7/8552 Carbon-Fiber/Epoxy

The experimental data for this FRP are obtained from [68]. In the simulations, specimens with holes from laminates of IM7/8552 carbon fiber/epoxy are loaded in tension and compression. The stacking sequence in the specimens are $[45_m/90_m/{-45}_m/0_m]$, where m is the number of ply blocks with the same orientation in the stack, as shown in Fig5.24.

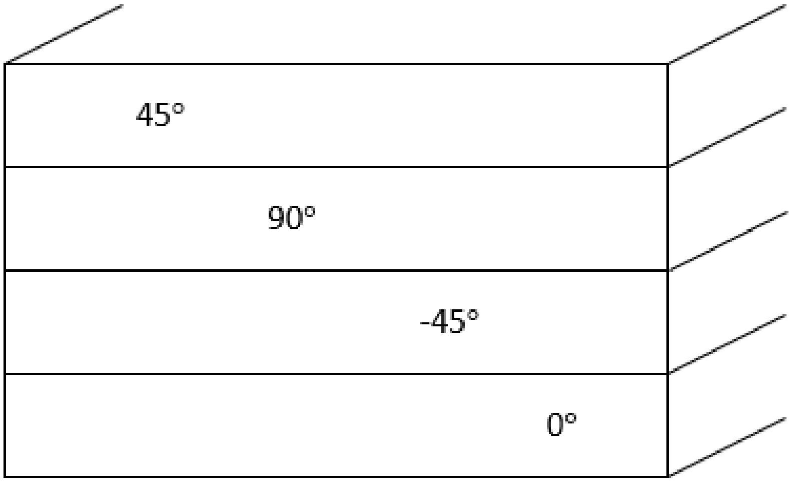

Figure 5.24: The stacking sequence for the test specimens of IM7/8552 carbon fiber/epoxy composite

The nominal thickness for each ply is 0.125mm. In Fig5.25, the test configuration is illustrated. The ratio of width-to-hole diameter is constant at 5 for all specimens. The length-to-hole diameter ratio is kept at 20 for tension and at 5 for compression. In the simulations, specimens without hole having three different thicknesses in tension and specimens with a hole of 3.175mm in diameter having the same three thicknesses are used. In compression, specimens without holes in three different thicknesses and two specimens with different thicknesses having a hole of 6.35mm in diameter are used.

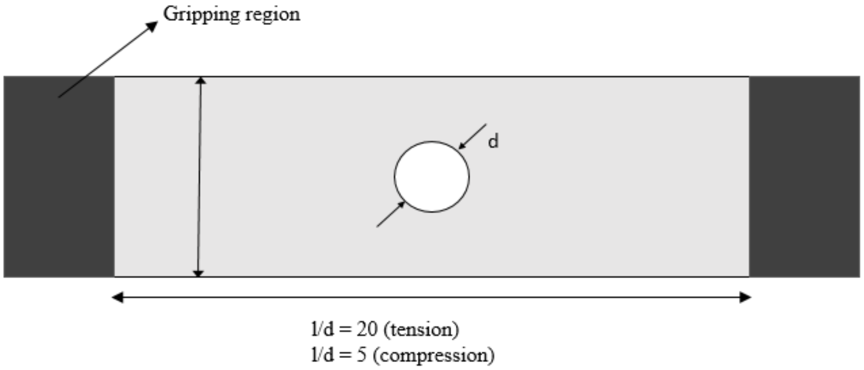

Figure 5.25: The open-hole strength test configuration for IM7/8552 Carbon-Fiber/Epoxy composite

In all simulations, the load is applied at a velocity of 0.01mm/s. The loading continues until the failure is reached. The element type is hexahedral, and the element size in the mesh is 0.125mm. The model is calibrated using the specimen without hole having a thickness of 8mm both in tension, Fig5.26, and in compression, Fig5.28. Once the parameter values are optimized, the predictions are carried out with the same optimal parameter values. The optimally calibrated parameter values for the FRP IM7/8552 carbon-fiber/epoxy are given in table 5.8.

Parameters	**Value**	**Parameters**	**Value**
C_1	400	k_7	0.011
C_2	100	k_8	0.02
C_3	50	k_9	0.015
C_4	50	s_1	0.01
C_5	0.439	s_2	0.015
C_6	0.439	s_3	0.0067
C_7	100	s_4	0.0039
C_8	200	s_5	0.002
C_9	50	s_6	0.0020
C_{10}	100	s_7	0.0025
C_{11}	120	h_1	1.5
k_1	0.0013	h_2	1.4
k_2	0.0128	h_3	0.5
k_3	0.031	h_4	0.5
k_4	0.044	h_5	1
k_5	0.02	h_6	0.5
k_6	0.0122	h_7	0.8

Table 5.8: The optimum parameter values for IM7/8552 Carbon-Fiber/Epoxy composite

In Fig5.26, the simulated strengths of the specimens with different thicknesses under tension are compared to the experimental values.

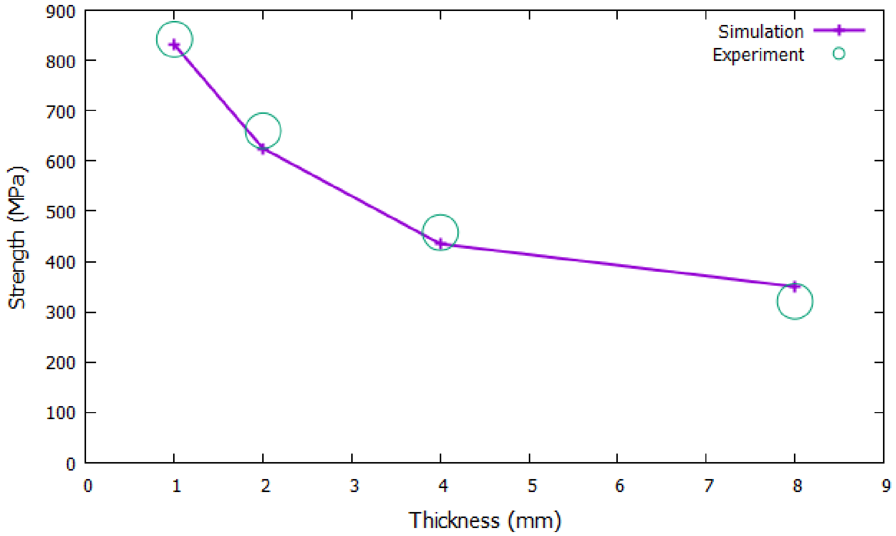

Figure 5.26: The model prediction and experimental tensile strengths for specimens without a hole

As shown in Fig5.26, the model predictions for specimens without hole under tension closely approximate the experimental data.

In Fig5.27, model predictions and experiment data for the strength of specimens with a hole under tension are compared. The hole size for all thicknesses is 3.175mm in this figure.

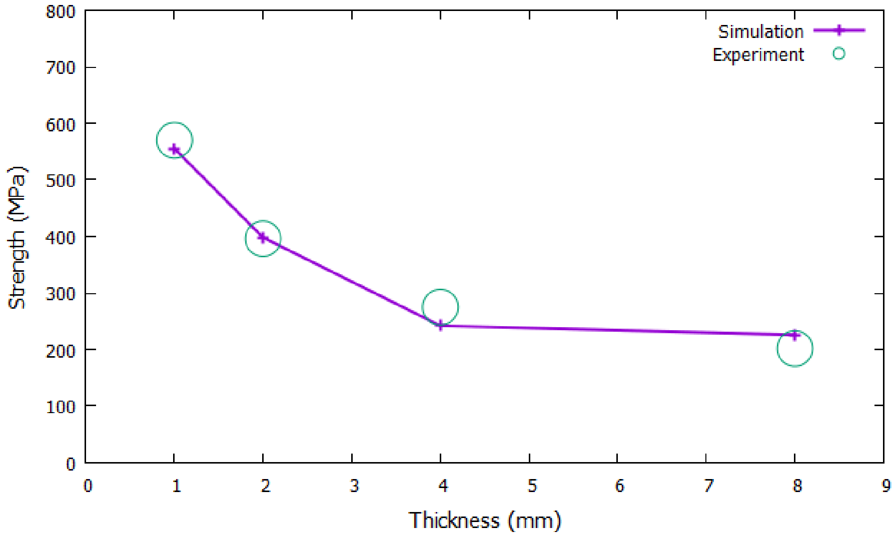

Figure 5.27: The model prediction and experimental tensile strengths for specimens with a hole

The Fig5.27 shows that the model predictions closely approximate the experimental results.

In Fig5.28 model predictions and experimental data for compressive strength of specimens without hole for three different thicknesses are compared.

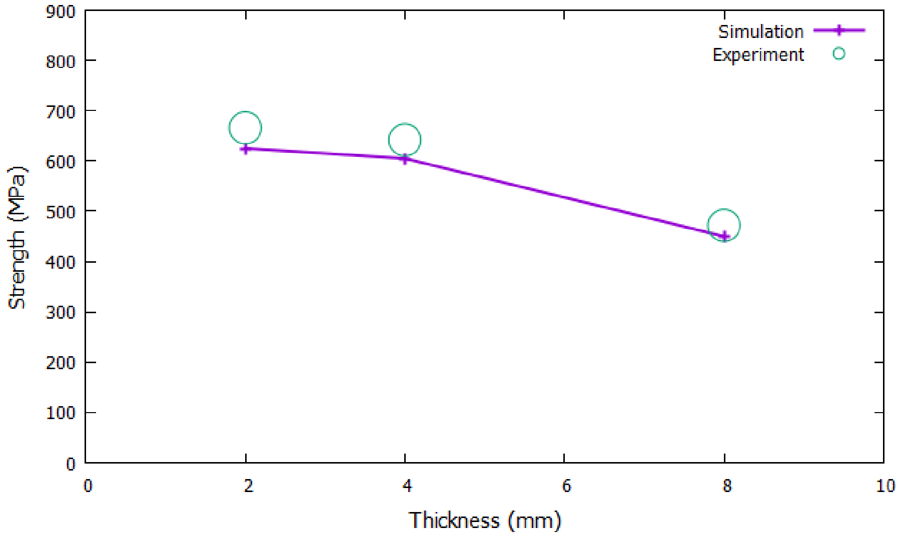

Figure 5.28: The model prediction and experimental compressive strengths for specimens without a hole

Figure 5.28 shows good agreement between model predictions and experimental data.

Model predictions and experimental data for specimens with a hole in compression having two thicknesses are shown in Fig5.29. The hole size in these simulations is 6.35mm in diameter.

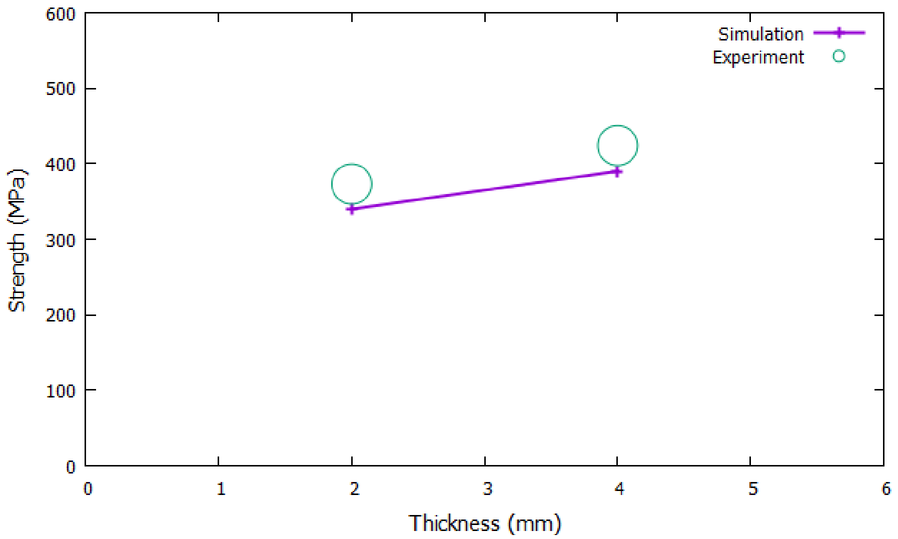

Figure 5.29: The model prediction and experimental compressive strengths for specimens with a hole

In Fig5.29, the model predictions and experimental data agree reasonably well.

The average error for Figs5.26, 5.27, 5.28 and 5.29 are 0.051, 0.072, 0.055 and 0.084. Thus, these results show that the cylindrical microplane model for transversely isotropic FRPs can predict both the tensile and compressive behaviors of open-hole laminates successfully. During the simulations in both tension and compression, two transverse cracks start from the top and bottom of the hole and propagate across the cross-section perpendicular to the loading. Figs5.30 and 5.31 illustrate predicted crack paths for both compression and tension for specimens with a thickness of 2 mm. The predicted crack paths are similar to the experimental data from [68]. The crack path obtained in tension is as expected, but in compression obtaining the same crack path instead of an inclined shear crack path is certainly interesting.

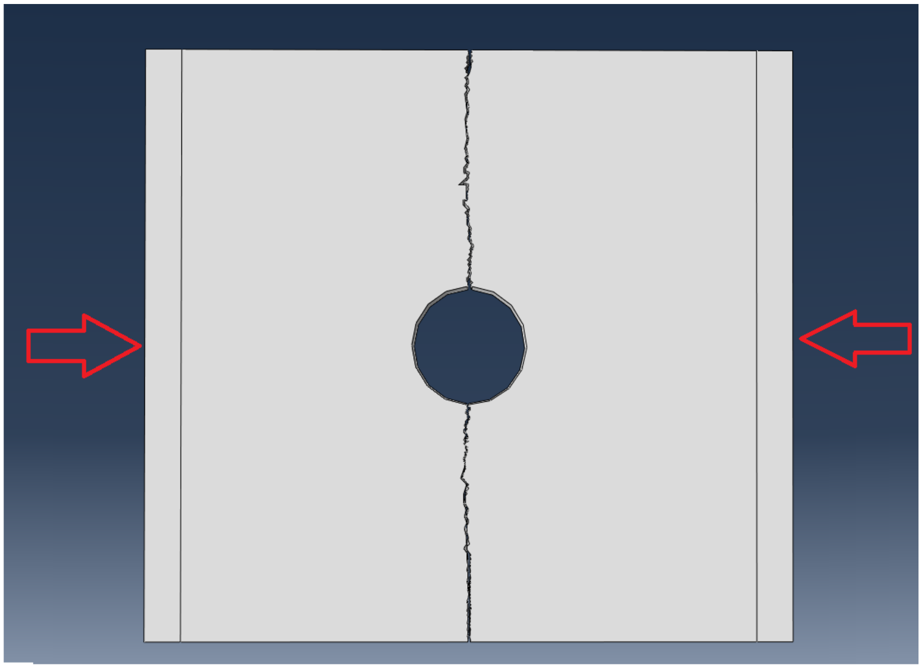

Figure 5.30: The predicted crack path by the model in compressive loading for the thickness of 2mm

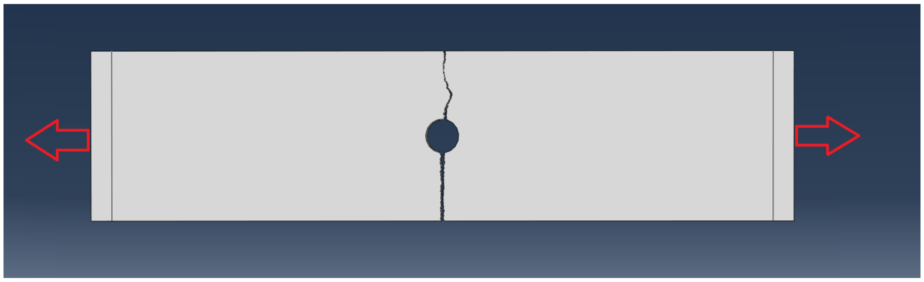

Figure 5.31: The predicted crack path by the model in tensile loading for the thickness of 2mm

Chapter 6

Conclusions

In view of the studies presented in this thesis, the following conclusions may be drawn:

1. Despite a number of existing theoretical and practical models for the failure of FRPs, there is pressing need for a robust model to predict the mechanical behavior of these materials in the general three-dimensional states of stress for the engineering analysis and design of numerous industrial products.

2. The concept of microplane model is attractive for FRPs due to their outstanding efficiency in bridging quasi-brittle micro-scale material behavior to macro-scale material behavior without jeopardizing applicability of the model to large scale finite element analyses.

3. The microplane model based on cylindrical geometry is an ideal approach among all possible microplane type approaches that captures the strongly anisotropic nonlinear behavior of FRPs.

4. The model can detect crack nucleation and branching and can simulates crack propagation correctly.

5. In the microplane model for transversely isotropic FRPs, the so-called stress-

strain boundaries, or strain-dependent yield limits, for longitudinal and transverse tension, compression, and shear have been developed.

6. The cylindrical microplane model is coded into a VUMAT subroutine for large scale simulations with the commercial finite element program Abaqus.
7. The model has been calibrated using experimental data on 4 different types of FRPs obtained from literature.
8. The model parameters are divided into fixed and free parameters, and a procedure for calibrating the model is developed using simple uniaxial test data for the unidirectional lamina for a given FRP.
9. The calibrated model has been used to predict very closely the biaxial failure envelope for two different unidirectional FRPs.
10. The model has been calibrated for and used to predict the size effect test data obtained using the 3-point bending tests of specimens with 4 different sizes made of laminated carbon fiber reinforced epoxy with a sequence of [-45/0/45/90].
11. The model has been calibrated for and used to predict the strength of specimens with a hole both in tension and in compression.
12. The predictions of the cylindrical microplane model for 4 different FRPs under 3 dimensional states of stress demonstrate the outstanding capability of the model in predicting the fracture of transversely isotropic FRPs.

Appendix

Vumat Code

```
subroutine vumat(
C Read only (unmodifiable)variables -
1 nblock, ndir, nshr, nstatev, nfieldv, nprops, lanneal,
2 stepTime, totalTime, dt, cmname, coordMp, charLength,
3 props, density, strainInc, relSpinInc,
4 tempOld, stretchOld, defgradOld, fieldOld,
5 stressOld, stateOld, enerInternOld, enerInelasOld,
6 tempNew, stretchNew, defgradNew, fieldNew,
C Write only (modifiable) variables -
7 stressNew, stateNew, enerInternNew, enerInelasNew )
C
include ’vaba_param.inc’
C
dimension props(nprops), density(nblock), coordMp(nblock,*),
1 charLength(nblock), strainInc(nblock,ndir+nshr),
2 relSpinInc(nblock,nshr), tempOld(nblock),
3 stretchOld(nblock,ndir+nshr),
```

```
4 defgradOld(nblock,ndir+nshr+nshr),
5 fieldOld(nblock,nfieldv), stressOld(nblock,ndir+nshr),
6 stateOld(nblock,nstatev), enerInternOld(nblock),
7 enerInelasOld(nblock), tempNew(nblock),
8 stretchNew(nblock,ndir+nshr),
8 defgradNew(nblock,ndir+nshr+nshr),
9 fieldNew(nblock,nfieldv),
1 stressNew(nblock,ndir+nshr), stateNew(nblock,nstatev),
2 enerInternNew(nblock), enerInelasNew(nblock)
C
character*80 cmname
real, parameter :: PI=3.141592653589793238462643383279 5d0
integer, parameter :: np=8, nvhm=3, nvhi=np*nvhm+1
real :: young, poisson,shearmodulus, fyoung,fpoisson,
$ alpha,beta,gamma,zeta
real :: k_1,k_2,k_3,k_4,k_5,k_6,k_7,k_8,k_9,
$ c_1, c_2, c_3, c_4, c_5,c_6,c_7,c_8,c_9,c_10,c_11,
$ h_1,h_2,h_3,h_4,h_5,h_6,s_1,s_2,s_3,s_4,s_5,s_6,s_7,h_7
real, dimension(1:6,1:np) :: qn, ql, qm
real, dimension(1:np) :: w
real, dimension(1:np) :: deps_N,deps_L,deps_M,eps_N,eps_L,
$eps_M,dsig_N,dsig_M,dsig_L,sig_N
real, dimension(1:np) :: enf,snf,sn0,emf,elf,sl0, sm0, slf,smf
real, dimension(1:np) :: snbt,snbc,smb,slb
real, dimension(1:nvhi+6) :: vh_ini, vh_fin ! additional hist. var. for element deletion
real, dimension(1:6,1:6) :: e
real, dimension(1:6) :: epsh,deps,depsh,eps,sig,dsig_elastic
```

```
real :: equivStress, fractureWorkInc, smean, stressPower
real :: eee,eeef,xnu,xnuf,shearm,th_del_1,th_del_2,seb,seq
integer :: ij(1:2,1:6), i, j, k,ic,inde,jp,inp
real, dimension(1:4,1:np) :: te
real, dimension(1:3) :: xn, xm, xl
real ::epsv,eqv,eqc,eqt,epsmax,epsmin,emmax,elmax,eql,eqm,eq
real, dimension(nblock,ndir+nshr) :: eps_vector
real, dimension(nblock,3) :: eigVal
NTENS = 6
young= props(1)
fyoung= props(2)
poisson= props(3)
fpoisson= props(4)
shearmodulus= props(5)
del=3.0d-2
c_1 = 3.0d2
c_2 = 1.0d2
c_3 = 5.0d1
c_4 = 5.0d1
c_5 = 0.5
c_6 = 0.5
c_7 = 1.0d2
c_8 =2.0d2
c_9 =5.0d1
c_10 =1.0d2
c_11 = 1.0d2
k_1 =1.0d-3
```

```
k_2 =1.0d-2
k_3 =3.0d-2
k_4 =3.0d-2
k_5 =2.0d-2
k_6 =2.0d-2
k_7 = 1.0d-2
k_8 =3.0d-2
k_9 =2.0d-2
s_1= 1.0d-2
s_2= 1.5d-2
s_3= 1.0d-2
s_4= 5.0d-3
s_5= 2.0d-3
s_6= 2.5d-3
s_7= 2.5d-3
h_1 =1.5d0
h_2 =1.5d0
h_3 =0.5d0
h_4 =0.5d0
h_5 =1.0d0
h_6 =0.5d0
h_7 =0.5d0
if(totalTime .eq. dt) then
e=0.0d0
eps=0.0d0
deps=0.0d0
eps_vector=0.0d0
```

```
eigVal = 0.0d0
deps_N = 0.0d0
deps_M = 0.0d0
deps_L = 0.0d0
eps_N = 0.0d0
eps_M = 0.0d0
eps_L = 0.0d0
stateOld = 0.0d0
end if
ij=reshape((/1,1,2,2,3,3,1,2,2,3,3,1/),(/2,6/))
if(np.eq.8) then
te = reshape((/0.0D0,1.0d0,0.0d0,0.65652875D0, ! 1st column
$0D0,0.803586195d0,-0.595188396d0,0.599777241D0, ! 2nd column
$0D0,0.803586195d0,0.595188396d0,0.599777241D0, ! 3
$0D0,0.394939378d0,-0.918707183d0,0.439360201D0, ! 4
$0D0,0.394939378d0,0.918707183d0,0.439360201D0, ! 5
$0D0,0.079855987d0,-0.996806411d0,0.203394509D0, ! 6
$0D0,0.079855987d0,0.996806411d0,0.203394509D0, ! 7
$1.0D0,0.0D0,0.0D0,1.5707963267948d0/),(/4,np/)) ! 8th column
end if
if(np.eq.25) then
te = reshape((/0.0D0,0.994943132d0,-0.100439858d0,0.200964847D0, ! 1st column
$0.0D0,0.994943132d0,0.100439858d0,0.200964847D0, ! 2nd column
$0.0D0,0.955278878d0,-0.295706383d0,0.197665014D0, ! 3
$0.0D0,0.955278878d0,0.295706383d0,0.197665014D0, ! 4
$0.0D0,0.88003346d0,-0.474911685d0,0.191119532D0, ! 5
$0.0D0,0.88003346d0,0.474911685d0,0.191119532D0, ! 6
```

```
$0.0D0,0.776694331d0,-0.629877699d0,0.181435879D0, ! 7
$0.0D0,0.776694331d0,0.629877699d0,0.181435879D0, ! 8
$0.0D0,0.654818644d0,-0.755786044d0,0.168773065D0, ! 9
$0.0D0,0.654818644d0,0.755786044d0,0.168773065D0, ! 10
$0.0D0,0.525054318d0,-0.851068718d0,0.15333902D0, ! 11
$0.0D0,0.525054318d0,0.851068718d0,0.15333902D0, ! 12
$0.0D0,0.396974891d0,-0.91782947d0,0.135387189D0, ! 13
$0.0D0,0.396974891d0,0.91782947d0,0.135387189D0, ! 14
$0.0D0,0.278991106d0,-0.960293686d0,0.115212384D0, ! 15
$0.0D0,0.278991106d0,0.960293686d0,0.115212384D0, ! 16
$0.0D0,0.177481525d0,-0.984124133d0,0.093145999D0, ! 17
$0.0D0,0.177481525d0,0.984124133d0,0.093145999D0, ! 18
$0.0D0,0.09681338d0,-0.995302552d0,0.069550838D0, ! 19
$0.0D0,0.09681338d0,0.995302552d0,0.069550838D0, ! 20
$0.0D0,0.039699296d0,-0.999211672d0,0.044817D0, ! 21
$0.0D0,0.039699296d0,0.999211672d0,0.044817D0, ! 22
$0.0D0,0.007571166d0,-0.999971338d0,0.019385558D0, ! 23
$0.0D0,0.007571166d0,-0.999971338d0,0.019385558D0, ! 24
$1.0D0,0.0D0,0.0D0,1.5707963267948d0/),(/4,np/))
end if
C ——————————————————
C ... Assemble tensors from direction cosines
C ——————————————————
qn = 0.0d0
ql = 0.0d0
qm = 0.0d0
w = 0.0d0
```

```
do jp=1,np

w(jp) =(2/pi) * te(4,jp)

xn(1) = te(3,jp)

xn(2) = te(2,jp)

xn(3) = te(1,jp)

xm(1)=1

xm(2)=0

xm(3)=0

xl(1)=0

xl(2)=xn(1)

xl(3)=-xn(2)

if(jp .eq. np) then

xl(3)=0

xl(2)=1

xl(1)=0

xm(3)=0

xm(2)=0

xm(1)=-1

end if

do k=1,6

IC=ij(1,k)

j=ij(2,k)

qn(k,jp) = xn(IC)*xn(j)

qm(k,jp) = 0.5D0*(xn(IC)*xm(j)+xn(j)*xm(IC))

ql(k,jp) = 0.5D0*(xn(IC)*xl(j)+xn(j)*xl(IC))

end do

end do
```

```
eee=young
eeef=fyoung
xnu=poisson
xnuf=fpoisson
shearm=shearmodulus
   e=0.0d0
e(1,1)=(eee**2*xnuf**2-eee*eeef)/((2*eee*xnu+2*eee)*xnuf**2+
$eeef*xnu**2-eeef)
e(1,2)=-(eee**2*xnuf**2+eee*eeef*xnu)/((2*eee*xnu+2*eee)*xnuf**2+
$eeef*xnu**2-eeef)
e(1,3)=-(eee*eeef*xnuf)/(2*eee*xnuf**2+eeef*xnu-eeef)
e(2,1)=-(eee**2*xnuf**2+eee*eeef*xnu)/((2*eee*xnu+2*eee)*xnuf**2+
$eeef*xnu**2-eeef)
e(2,2)=(eee**2*xnuf**2-eee*eeef)/((2*eee*xnu+2*eee)*xnuf**2+
$eeef*xnu**2-eeef)
e(2,3)=-(eee*eeef*xnuf)/(2*eee*xnuf**2+eeef*xnu-eeef)
e(3,1)=-(eee*eeef*xnuf)/(2*eee*xnuf**2+eeef*xnu-eeef)
e(3,2)=-(eee*eeef*xnuf)/(2*eee*xnuf**2+eeef*xnu-eeef)
e(3,3)=(eeef**2*xnu-eeef**2)/(2*eee*xnuf**2+eeef*xnu-eeef)
e(4,4)=eee/(xnu+1)
e(5,5)=2*shearm
e(6,6)=2*shearm
do i = 1, nblock
vh_ini = stateOld(i,:)
deps=strainInc(i,:)
eps(1)=vh_ini(nvhi+1)
eps(2)=vh_ini(nvhi+2)
```

```
eps(3)=vh_ini(nvhi+3)
eps(4)=vh_ini(nvhi+4)
eps(5)=vh_ini(nvhi+5)
eps(6)=vh_ini(nvhi+6)
epsh=eps
epsh(4)=2*eps(4)
epsh(5)=2*eps(5)
epsh(6)=2*eps(6)
depsh(4)=2*deps(4)
depsh(5)=2*deps(5)
depsh(6)=2*deps(6)
C ——————
C ... Initializations
C ——————
eps_N = matmul( epsh,qn)
eps_L = matmul( epsh,ql)
eps_M = matmul( epsh,qm)
deps_N = matmul(depsh,qn)
deps_L = matmul(depsh,ql)
deps_M = matmul(depsh,qm)
dsig_elastic=matmul(e,deps)
dsig_elastic(4)=2*dsig_elastic(4)
dsig_elastic(5)=2*dsig_elastic(5)
dsig_elastic(6)=2*dsig_elastic(6)
dsig_N=matmul( dsig_elastic,qn)
dsig_M=matmul( dsig_elastic,qm)
dsig_L=matmul( dsig_elastic,ql)
```

```
sn0 = vh_ini(2:nvhi:nvhm)
sm0 = vh_ini(3:nvhi:nvhm)
sl0 = vh_ini(4:nvhi:nvhm)
enf=eps_N+deps_N
emf=eps_M+deps_M
elf=eps_L+deps_L
snf=sn0+dsig_N
smf=sm0+dsig_M
slf=sl0+dsig_L
do k=1,np
if(abs(eps_N(k))>(deps_N(k))) then
if(abs(eps_N(k)+deps_N(k))<abs(eps_N(k))) then
snf(k) =(sn0(k)/eps_N(k))*(eps_N(k)+deps_N(k))
else
snf(k)=sn0(k)+dsig_N(k)
end if
end if
if(abs(eps_M(k))>(deps_M(k))) then
if(abs(eps_M(k)+deps_M(k))<abs(eps_M(k))) then
smf(k) =(sm0(k)/eps_M(k))*(eps_M(k)+deps_M(k))
else
smf(k)=sm0(k)+dsig_M(k)
end if
end if
if(abs(eps_L(k))>(deps_L(k))) then
if(abs(eps_L(k)+deps_L(k))<abs(eps_L(k))) then
slf(k) =(sl0(k)/eps_L(k))*(eps_L(k)+deps_L(k))
```

```
else
slf(k)=sl0(k)+dsig_L(k)
end if
end if
end do
do inde=1 , np-1
epsmax=max(enf(inde),epsmax)
epsmin=min(enf(inde),epsmin)
end do
epsv= (eps(1)+deps(1)+deps(2)+eps(2))
if(epsv> = 0) then
eqv=max(0.0d0,c_1*(epsv-k_1))
else
eqv=max(0.0d0,c_2*(abs(epsv)-k_2))
end if
eqt=max(0.0d0,c_3*(abs(epsmax)-k_3))
eqc=max(0.0d0,c_4*(abs(epsmin)-k_4))
do inde=1 ,np-1
snbt(inde) = )c_5/young) * (h_1 *enf(inde)+s_1)*exp(-(eqt+eqv))
snbc(inde) = (c_6/young) * (h_2 *abs(enf(inde))+s_2)*exp(-(eqc+eqv))
end do
inde= np
if(enf(inde)> = 0) then
eqv=max(0.0d0,c_7*(enf(inde)+(young/fyoung)*abs(epsv)-k_5))
else
eqv=max(0.0d0,c_8*(abs(enf(inde))+(young/fyoung)*abs(epsv)-k_6))
end if
```

```
snbt(inde) = fyoung * (h_3 *enf(inde)+s_3)*exp(-(eqv))
snbc(inde) = fyoung * (h_4 *abs(enf(inde))+s_4)*exp(-(eqv))
do ic=1,np
if(snf(ic)< =0) then
snf(ic) = max(snf(ic),-snbc(ic))
else
snf(ic) = min(snf(ic),snbt(ic))
end if
end do
do inde=1 , np-1
emmax=max(abs(emf(inde)),emmax)
elmax=max(abs(elf(inde)),elmax)
end do
epsv= (eps(1)+eps(2)+deps(1)+deps(2))
if(epsv> =0) then
eqv=max(0.0d0,c_1*(epsv-k_1))
else
eqv=max(0.0d0,c_2*(abs(epsv)-k_2))
end if
eql=max(0.0d0,c_9*(elmax-k_7))
eqm=max(0.0d0,c_10*(emmax-k_8))
do inde=1 , np-1
slb(inde)=(young/(poisson+1))*(h_5*abs(elf(inde))+s_5)*
$exp(-(eql+eqv))
smb(inde) =(2*shearmodulus)*(h_6*abs(emf(inde))+s_6)*exp(-(eqm+
$eqv))
end do
```

```
inde= np
     eq=max(0.0d0,c_11*(sqrt((elf(inde))**2+(emf(inde))**2)-k_9))
seb =(2*shearmodulus)*(h_7 *sqrt((elf(inde))**2
$+(emf(inde))**2)+s_7)*exp(-(eq))
do inde= 1 , np-1
     if(abs(slf(inde))> = slb(inde)) then
     slf(inde)=sign(slb(inde),slf(inde))
end if
     if(abs(smf(inde))> = smb(inde)) then
     smf(inde)=sign(smb(inde),smf(inde))
end if
end do
inde= np
     seq=sqrt((smf(inde)**2)+(slf(inde))**2)
     if(seq > seb) then
     smf(inde)=(smf(inde)/seq)*seb
     slf(inde)=(slf(inde)/seq)*seb
     end if
     eps_vector(i,1)=(eps(1)+deps(1))
eps_vector(i,2)=(eps(2)+deps(2))
eps_vector(i,3)=0.0d0
eps_vector(i,4)=(eps(4)+deps(4))
eps_vector(i,5)=0.0d0
eps_vector(i,6)=0.0d0
call vsprinc( nblock, eps_vector, eigVal, ndir, nshr )
maxp=0.0d0
maxp = max(abs(eigVal(i,1)) ,abs(eigVal(i,2)))
```

```
maxp = max(maxp ,abs(eigVal(i,3)))
if ( maxp >th_del_1) then
vh_fin(1)=0
else
vh_fin(1)=1
end if
eps_vector(i,1)=(eps(1)+deps(1))
eps_vector(i,2)=(eps(2)+deps(2))
eps_vector(i,3)=(eps(3)+deps(3))
eps_vector(i,4)=(eps(4)+deps(4))
eps_vector(i,5)=(eps(5)+deps(5))
eps_vector(i,6)=(eps(6)+deps(6))
call vsprinc( nblock, eps_vector, eigVal, ndir, nshr )
    vh_fin(1)=1
    do inp=1 , 3
    if ( eigVal(i,inp)> = del) then
vh_fin(1)=0
    else
vh_fin(1)=1
end if
    end do
sig = (matmul(qn,snf*w) + matmul(qm,smf*w) + matmul(ql,slf*w))
C ————————————————————-
C ... Update microplane normal and shear stresses
C ————————————————————-
vh_fin(2:nvhi:nvhm) = snf
vh_fin(3:nvhi:nvhm) = smf
```

```
vh_fin(4:nvhi:nvhm) = slf
vh_fin(nvhi+1)=(eps(1)+deps(1))
vh_fin(nvhi+2)=(eps(2)+deps(2))
vh_fin(nvhi+3)=(eps(3)+deps(3))
vh_fin(nvhi+4)=(eps(4)+deps(4))
vh_fin(nvhi+5)=(eps(5)+deps(5))
vh_fin(nvhi+6)=(eps(6)+deps(6))
stateNew(i,:)=vh_fin
stressNew(i,:)=sig
C ! Update the specific internal energy -
stressPower = (( stressOld(i,1)+stressNew(i,1) )*
$ strainInc(i,1) + ( stressOld(i,2)+stressNew(i,2) )*
$ strainInc(i,2) + ( stressOld(i,3)+stressNew(i,3) )*
$ strainInc(i,3) + 2.0*( stressOld(i,4)+stressNew(i,4) )*
$ strainInc(i,4) )/2.0
enerInternNew(i) = enerInternOld(i) + stressPower / density(i)
C
C ! Update the dissipated inelastic specific energy -
smean = ( stressNew(i,1) + stressNew(i,2) +
$ stressNew(i,3) )/3.0
equivStress = sqrt( 3.0/2.0 * ( (stressNew(i,1)-smean)**2 +
$ (stressNew(i,2)-smean)**2 + (stressNew(i,3)-smean)**2 +
$ two * stressNew(i,4)**2 ) )
fractureWorkInc = stressNew(i,1)*deps(1) +
$ stressNew(i,2)*deps(2) + stressNew(i,3)*deps(3) +
$ stressNew(i,4)*deps(4) + stressNew(i,5)*deps(5) +
$ stressNew(i,6)*deps(6)
```

```
enerInelasNew(i) = enerInelasOld(i)+fractureWorkInc/density(i)

end do

return

end subroutine vumat
```

Bibliography

[1] S. Prashanth, K. Subbaya, K. Nithin, and S. Sachhidananda, “Fiber reinforced composites - A review,” *Journal of Material Sciences and Engineering*, vol. 6, no. 3, pp. 1–6, 2017.

[2] H. M. Akil, M. F. Omar, M. A. A. Mazuki, S. Safiee, Z. Ishak, and A. Abu Bakar, “Kenaf fiber reinforced composites: A review,” *Materials and Design*, vol. 32, no. 8-9, pp. 4107–4121, 2011.

[3] Červenka Consulting, “Commercial software package atena.” `https://www.cervenka.cz`.

[4] R. Petersen, *Micromechanics & Fiber-Reinforced Composites in Biomedical Research*. Vdm Verlag, 2008.

[5] B. Cheung and J. Carey, *Handbook of Advances in Braided Composite Materials*, ch. Macromechanics of composite materials, pp. 307–319. Woodhead Publishing, 2017.

[6] R. M. Jones., *Mechanics of Composite Materials*, ch. Classification and Characteristics of Composite Materials, pp. 3–5. Taylor and Francis, 1999.

[7] R. M. Jones., *Mechanics of Composite Materials*. Virginia: Taylor and Francis, 1999.

[8] Y. Karnakar and K. Madh, "Experimental analysis on glass/epoxy composite beams," *International Journal of Innovative Science*, vol. 2, no. 12, pp. 24–41, 2015.

[9] A. K. Kaw, *Mechanics of Composite Materials*. London: Taylor and Francis, 2006.

[10] Z. P. Bažant, Y. Xi, and S. G. Reid, "Statistical size effect in quasi-brittle structures: I. Is Weibull theory applicable?," *Journal of Engineering Mechanics*, vol. 117, no. 11, pp. 2609–2622, 1991.

[11] Z. P. Bažant, Y. Zhou, G. Zi, and I. M. Danie, "Size effect and asymptotic matching analysis of fracture of closed-cell polymeric foam," *International Journal of Solids and Structures*, vol. 40, no. 25, pp. 7197–7217, 2003.

[12] Z. P. Bažant, Y. Zhou, G. Zi, D. Novák, and I. M. Danie, "Size effect on flexural strength of fiber-composite laminates," *Journal of Engineering Materials and Technology*, vol. 126, no. 1, pp. 29–37, 2004.

[13] Z. Goangseup and Z. P., "Eigenvalue method for computing size effect of cohesive cracks with residual stress, with application to kink-bands in composites," *International Journal of Engineering Science*, vol. 41, no. 13-14, pp. 1519–1534, 2003.

[14] G. Cusatis, A. Beghini, and Z. P. Bažant, "Spectral stiffness microplane model for quasibrittle composite laminates Part I: Theory," *Journal of Applied Mechanics*, vol. 75, no. 2, pp. 210091–210099, 2008.

[15] B. Rosen, *Mechanics of Composite Strengthening: Fibre Composite Materials*, ch. 3, pp. 37–75. American Society of Metals, 1956.

[16] E. M. Odom and D. F. Adams, “Failure modes of unidirectional carbon/epoxy composite compression specimens,” *Composites*, vol. 21, no. 4, pp. 289–296, 1990.

[17] H. Hahn and J. G. Williams, “Compression failure mechanisms in unidirectional composites,” in *in ASTM Symp. on Composite Mater*, (Philadelphia), Pa, 1984.

[18] J. M. Hedgepeth and P. V. Dyke, “Local stress concentrations in imperfect filamentary composite materials,” *Journal of Composite Materials*, vol. 1, no. 3, pp. 294–309, 1967.

[19] Z. Xia, W. Curtin, and T. Okabe, “Green’s function vs. shear-lag models of damage and failure in fiber composites,” *Composites Science and Technology*, vol. 62, no. 10-11, pp. 1279–1288, 2002.

[20] Z. Xia, T. Okabe, and W. Curtin, “Shear-lag versus finite element models for stress transfer in fiber-reinforced composites,” *Composites Science and Technology*, vol. 62, no. 9, pp. 1141–1149, 2002.

[21] H. Fukuda, “Stress concentration factors in unidirectional composites with random fiber spacing,” *Composites Science and Technology*, vol. 22, no. 2, p. 153–163, 1985.

[22] W. Weibull, “A statistical distribution function of wide applicability,” *Journal of Applied Mechanics*, vol. 18, no. 3, pp. 293–297, 1951.

[23] Y. Y. Yang, Y. Liu, and Z. Ran, “Microscopic failure mechanisms of fiber-reinforced polymer composites under transverse tension and compression,” *Composites Science and Technology*, vol. 72, no. 15, pp. 1818–1825, 2012.

[24] D. M. Blackketter and D. Upadhyaya, “Micromechanics prediction of the transverse tensile strength of carbon fiber/epoxy composites: The influence of the matrix and interface,” *Polymer Composites*, vol. 14, no. 5, pp. 437–446, 1993.

[25] L. E. Asp, L. A. Berglund, and R. Talreja, “Prediction of matrix-initiated transverse failure in polymer composites,” *Polymer Composites*, vol. 56, no. 9, pp. 1089–1097, 1996.

[26] V. Chohan and C. Galiotis, “Effects of interface, volume fraction and geometry on stress redistribution in polymer composites under tension,” *Composites Science and Technology*, vol. 57, no. 8, pp. 1089–1101, 1997.

[27] B. W. Rosen, “Tensile failure of fibrous composites,” *AIAA Journal*, vol. 2, no. 11, pp. 1985–1991, 1964.

[28] A. S. Argon, “Fracture of composites,” *Treatise on Materials Science and Technology*, vol. 1, pp. 79–114, 1972.

[29] B. Budiansky and N. A. Fleck, “Compressive failure of fibre composites,” *Journal of the Mechanics and Physics of Solids*, vol. 41, no. 1, pp. 183–211, 1993.

[30] C. González and J. LLorca, “Mechanical behavior of unidirectional fiber-reinforced polymers under transverse compression: Microscopic mechanisms and modeling,” *Composites Science and Technology*, vol. 67, no. 13, pp. 2795–2806, 2007.

[31] D. F. Adams and D. R. Doner, “Longitudinal shear loading of a unidirectional composite,” *Journal of Composite Materials*, vol. 1, no. 4, pp. 4–17, 1967.

[32] S. W. Tsai and E. M. Wu, “A general theory of strength for anisotropic materials,” *Journal of Composite Materials*, vol. 5, no. 1, pp. 58–80, 1971. doi: `10.1177/002199837100500106`.

[33] H. Lapczyk and J. A. Hurtado, “Progressive damage modeling in fiber-reinforced materials,” *Composites: Part A*, vol. 38, pp. 2333–2341, 2007.

[34] E. Totry, C. Gonzalez, and J. Llorca, “Prediction of the failure locus of C/PEEK composites under transverse compression and longitudinal share through

computational micromechanics," *Composites Science and Technology*, vol. 68, pp. 3128–3136, 2008.

[35] X. S. Sun, V. B. C. Tan, and T. E. Tay, "Micromechanics-based progressive failure analysis of fibre-reinforced composites with non-iterative element-failure method," *Computers and Structures*, vol. 89, pp. 1103–1116, 2011.

[36] P. P. Camanho, M. A. Bessa, G. Catalanotti, M. Vogler, and R. Rolfes, "Modeling the inelastic deformation and fracture of polymer composites - Part II: Smeared crack model," *Mechanics of Materials*, vol. 59, pp. 36–49, 2013.

[37] F. van der Meer, "Micromechanical validation of a mesomodel for plasticity in composites," *European Journal of Mechanics - A/Solids*, vol. 60, pp. 58–69, 2016.

[38] S. Zhou, Y. Sun, B. Chen, and T. E. Tay, "Progressive damage simulation of open-hole composite laminates under compression based on different failure criteria," *Journal of composite materials*, vol. 51, no. 9, pp. 1239–1251, 2017.

[39] G. I. Taylor, "Plastic strain in metals," *Journal of the Institute of Metals*, vol. 62, pp. 307 – 324, 1949. doi: `10.1016/j.pmatsci.2013.06.001`.

[40] S. B. Batdorf and B. Budiansky, "A mathematical theory of plasticity based on the concept of slip," Tech. Rep. 1871, National Advisory Committee, Washington, D. C., 1949. `https://digital.library.unt.edu/ark:/67531/metadc55196/m2/1/high_res_d/19930082547.pdf`.

[41] G. C. Butler and D. L. Mc Dowell, "Polycrystal constraint and grain subdivision," *International Journal of Plasticity*, vol. 14, no. 8, pp. 703–717, 1998.

[42] B. Budiansky, "Theoretical prediction of plastic strains of polycrystals," in *Proceedings of the fourth U.S. National Congress of Applied Mechanics, ASME*, (New York), pp. 1175–1185, 1962.

[43] J. R. Rice, "On the structure of stress-strain relations for timedependent plastic deformation of metals," *Journal of Applied Mechanics*, vol. 37, no. 3, pp. 728–737, 1970.

[44] Z. P. Bažant, *Mechanics of engineering materials*, ch. Microplane model for strain-controlled inelastic behavior, pp. 45–49. London: Wiley, 1984.

[45] Z. Bažant and J. Planas, *Fracture and size effect in concrete and other quasibrittle materials*. CRC Press, London, 1997.

[46] Z. P. Bažant, *Scaling of structural strength*. Hermes- Penton Science Ltd., London, 2005.

[47] F. C. Caner and Z. P. Bažant, "Microplane model M7 for plain concrete. I: Formulation," *Journal of Engineering Mechanics*, vol. 139, no. 12, pp. 1714–1723, 2013.

[48] F. C. Caner and Z. P. Bažant, "Microplane model M7 for plain concrete. II: Calibration and verification," *Journal of Engineering Mechanics*, vol. 139, no. 12, pp. 1724–1735, 2013.

[49] C. Li, F. C. Caner, V. T. Chau, and Z. P. Bažant, "Spherocylindrical microplane constitutive model for shale and other anisotropic rocks," *Journal of the Mechanics and Physics of Solids*, vol. 103, pp. 155–178, 2017.

[50] A. Beghini, G. Cusatis, and Z. P. Bažant, "Spectral stiffness microplane model for quasibrittle composite laminates Part II: Calibration and validation," *Journal of Applied Mechanics*, vol. 75, no. 2, pp. 210101–210106, 2008.

[51] F. C. Caner, Z. P. Bažant, C. Hoover, A. Waas, and K. Shahwan, "Microplane model for fracturing damage of triaxially braided fiber-polymer composites," *ASME J. of Engineering Materials and Technology*, vol. 133, pp. 021024–1–021024–12, 2011.

[52] K. Kirane, M. Salviato, and Z. P. Bažant, “Microplane triad model for simple and accurate prediction of orthotropic elastic constants of woven fabric composites,” *Journal of Composite Materials*, vol. 50, no. 9, pp. 1247–1260, 2015.

[53] F. C. Caner and I. Carol, “Microplane consitutive model and computational framework for blood vessel tissue,” *ASME Journal of Biomechanical Engineering*, vol. 128, pp. 419–427, 2006.

[54] F. C. Caner, Z.-Y. Guo, B. Moran, and B. Z. P., “Hyperelastic anisotropic microplane constitutive model for annulus fibrosus,” *Journal of Biomechanical Engineering*, vol. 129, no. 5, pp. 632–641, 2007.

[55] J. Vorel, M. Marcon, G. Cusatis, F. Caner, G. di Luzio, and R. Wan-Wendner, “A comparison of the state of the art models for constitutive modelling of concrete,” *Computers & Structures*, vol. 244, p. 106426, 2021.

[56] H. T. Nguyen, F. C. Caner, and Z. P. Bažant, “Conversion of explicit microplane model with boundaries to a constitutive subroutine for implicit finite element programs,” *International Journal for Numerical Methods in Engineering*, 2020.

[57] Z. P. Bažant, Y. Xiang, and P. C. Prat, “Microplane model for concrete. i: Stress-strain boundaries and finite strain,” *Journal of Engineering Mechanics*, vol. 122, no. 2, pp. 255–262, 1996.

[58] Z. P. Bažant and B. H. Oh, “Microplane model for fracture analysis of concrete structures,” *Proc., Symp. on Interaction of Non-Nuclear Munitions with Struct*, p. 49–53, 1983.

[59] Z. P. Bažant and P. C. Prat, “Microplane model for brittle-plastic material: I. theory,” *Journal of Engineering Mechanics*, vol. 114, no. 10, p. 1672–1688, 1988.

[60] Z. P. Bažant and L. Cedolin, *Stability of Structures Elastic, Inelastic, Fracture, and Damage Theories*. New York: Dover Publications, 2003.

[61] Z. P. Bažant, F. C. Caner, I. Carol, M. D. Adley, and S. A. Akers, “Microplane model m4 for concrete i: Formulation with work-conjugate deviatoric stress,” *Journal of Engineering Mechanics*, vol. 126, no. 9, pp. 944–953, 2000.

[62] R. Gautam and R. C. Wong, “Transversely isotropic stiffness parameters and their measurement in colorado shale,” *Canadian Geotechnical Journal*, vol. 43, no. 12, p. 1290–1305, 2006.

[63] G. A. Waters, R. E. Lewis, and D. C. Bentley, “The effect of mechanical properties anisotropy in the generation of hydraulic fractures in organic shales,” in *in SPE Annual Technical Conference*, (Denver, Colorado), Society of Petroleum Engineers, 2011.

[64] P. Davis and P. Rabinowitz, “Abscissas and weights for gaussian quadratures of high order,” *Journal of Research of the National Bureau of Standards*, vol. 56, pp. 35–37, 1956.

[65] P. D. Soden, M. J. Hinton, and A. S. Kaddour, “Lamina properties, lay-up configurations and loading conditions for a range of fibre-reinforced composite laminates,” *Composites Science and Technology*, vol. 58, no. 7, pp. 1011–1022, 1998.

[66] P. D. Soden, M. J. Hinton, and A. S. Kaddour, “Biaxial test results for strength and deformation of a range of e-glass and carbon fibre reinforced composite laminates: failure exercise benchmark data,” *Composites Science and Technology*, vol. 62, no. 12–13, pp. 1489–1514, 2002.

[67] S. S. Rudraraju, A. Salvi, K. Garikipati, and A. M. Waas, “In-plane fracture of laminated fiber reinforced composites with varying fracture resistance: Experimental observations and numerical crack propagation simulations,” *International Journal of Solids and Structures*, vol. 47, pp. 901–911, 2010.

[68] M. R. Wisnom, S. R. Hallett, and C. Soutis, “Scaling effects in notched composites,” *Journal of Composite Materials*, vol. 44, no. 2, pp. 195–210, 2010.

[69] S. A. Crasto, R. Y. Kim, and J. M. Whitney, “A new test method to determine the compressive strength of fiber-reinforced composites,” in *AGARD Report 785* (NATO, ed.), 1991. Fig. 5, ISBN-92-835-0666-9/AD-A253004, `https://www.sto.nato.int/publications/AGARD/AGARD-R-785/AGARD-R-785.pdf`.

[70] H.-B. Hellweg and M. Crisfield, “A new arc-length method for handling sharp snap-backs,” *Computers & Structures*, vol. 66, no. 5, pp. 704–709, 1998.